Molecular basis for plasma membrane recruitment of PI4KA by EFR3

Sushant Suresh[1]*, Alexandria L Shaw[1,2]*, Joshua G Pemberton[3,4], Mackenzie K Scott[1], Noah J Harris[1], Matthew AH Parson[1], Meredith L Jenkins[1], Pooja Rohilla[3], Alejandro Alvarez-Prats[3], Tamas Balla[3], Calvin K Yip[2#], John E Burke[1,2#]

[1] Department of Biochemistry and Microbiology, University of Victoria, Victoria, BC, V8W 2Y2, Canada

[2] Department of Biochemistry and Molecular Biology, The University of British Columbia, Vancouver, BC, V6T 1Z3, Canada

[3] Section on Molecular Signal Transduction, Eunice Kennedy Shriver National Institute of Child Health and Human Development, National Institutes of Health, Bethesda, MD, United States.

[4] Current address: Department of Biology, Western University, London, ON, N6A 3K7 Canada

* These authors contributed equally

[#]Corresponding authors: Calvin K Yip calvin.yip@ubc.ca, John E Burke jeburke@uvic.ca: Lead contact: John E Burke jeburke@uvic.ca

Abstract

The lipid kinase phosphatidylinositol 4 kinase III alpha (PI4KIIIα/PI4KA) is a master regulator of the lipid composition and asymmetry of the plasma membrane. PI4KA exists primarily in a heterotrimeric complex with its regulatory proteins TTC7 and FAM126. Fundamental to PI4KA activity is its targeted recruitment to the plasma membrane by the lipidated proteins EFR3A and EFR3B. Here, we report a cryo-EM structure of the C-terminus of EFR3A bound to the PI4KA-TTC7B-FAM126A complex, with extensive validation using both hydrogen deuterium exchange mass spectrometry (HDX-MS), and mutational analysis. The EFR3A C-terminus undergoes a disorder-order transition upon binding to the PI4KA complex, with an unexpected direct interaction with both TTC7B and FAM126A. Complex disrupting mutations in TTC7B, FAM126A, and EFR3 decrease

PI4KA recruitment to the plasma membrane. Multiple post-translational modifications and disease linked mutations map to this site, providing insight into how PI4KA membrane recruitment can be regulated and disrupted in human disease.

One sentence summary

The cryo-EM structure of the C-terminus of EFR3A bound to the PI4KA complex reveals the molecular mechanism underlying PI4KA membrane localisation, and provides novel insight into PI4KA regulation and its involvement in human disease.

Introduction

Phosphoinositide lipids play numerous roles in myriad cellular functions (*1–3*). One of the most abundant phosphoinositide lipids is the molecule phosphatidylinositol 4-phosphate (PI4P) (*4*), which can be generated by four different lipid kinases in humans (encoded by the genes *PI4KA, PI4KB, PI4K2A,* and *PI4K2B*), with PI4KA generating the primary pool of PI4P at the plasma membrane (PM) (*5*). PI4P is essential for defining the identity of the PM, as it is the precursor for the signaling lipids phosphatidylinositol (4,5)-bisphosphate (PI(4,5)P_2) and phosphatidylinositol (3,4,5)-trisphosphate (PIP_3), regulates the non-vesicular transport of phosphatidylserine (*6*), and is also a substrate of the phospholipase C (PLC) pathway (*7*). Dysregulation of PI4KA is involved in multiple human diseases (*8*), with loss of function mutations in PI4KA or its regulatory proteins being causative of neurological (*9*, *10*), immunological (*11*), and gastrointestinal disorders (*12*, *13*). PI4KA and its regulatory proteins have also been shown to be critical for cancer growth (*14*, *15*) and viral infection (*16*).

PI4KA shares an evolutionary history with the class I-III PI 3-kinases (PI3Ks) and PI4KB, with a central feature of regulation for all of these enzymes being that they are recruited to membrane surfaces by specific lipid or protein binding partners (*17*). PI4KA primarily exists in cells as a complex with the regulatory proteins TTC7 (two isoforms TTC7A and TTC7B) and FAM126 (two isoforms FAM126A and FAM126B) (*18*, *19*). PI4KA and TTC7 are conserved throughout all eukaryotes, while FAM126 is found in most metazoans, with it not being found in fungi, but found in organisms containing a simple

60 nervous system (*20*). Analysis of the PI4KA-TTC7-FAM126 complex using cryogenic
61 electron microscopy (cryo-EM) and hydrogen deuterium exchange mass spectrometry
62 (HDX-MS) showed that it assembles into a large ~750 kDa complex (*18*, *21*). PI4KA self-
63 assembles through its dimerization domain leading to a dimer of heterotrimers, which we
64 will refer to as the PI4KA complex. FAM126 does not bind to PI4KA directly but instead
65 acts as a stabilizer of TTC7, which binds to PI4KA (*19*). The most well-established
66 mechanism of membrane recruitment is through the binding of the palmitoylated protein
67 EFR3 to TTC7 (*5*). However, the exact molecular mechanism underlying EFR3-mediated
68 PM recruitment of the PI4KA complex has remained elusive (*5*, *22*, *23*).

69 The interaction between EFR3 and TTC7 has been extensively studied in yeast,
70 where the protein Ypp1 (yeast ortholog of TTC7) binds to the disordered C-terminus of
71 Efr3 (yeast homolog of EFR3) (*24*, *25*). In yeast, this interaction is regulated by
72 phosphorylation of the C-terminus of Efr3, with phosphorylation disrupting Ypp1-mediated
73 PM recruitment of Stt4 (yeast homolog of PI4KA) (*25*). It has been challenging to
74 extrapolate these results to derived eukaryotic lineages, including humans, as the C-
75 terminus of EFR3 is only partially conserved between yeast and humans. As PI4KA
76 activity needs to be upregulated upon PLC signaling to maintain the PM pool of PI4P (*26*),
77 there likely are unknown regulatory mechanisms controlling EFR3-mediated recruitment
78 in vertebrates. Defining the molecular mechanism of EFR3-mediated PM recruitment of
79 PI4KA is essential to understanding possible regulatory mechanisms controlling the
80 activity of the PI4KA complex through association with the PM.

81 To fully explore the molecular mechanisms of how EFR3 can bind to and regulate
82 the PI4KA complex, we have used a synergistic application of cryo-EM and HDX-MS. Our
83 structural analyses reveal that EFR3A interacts with the PI4KA complex through an
84 evolutionarily conserved region within the C-terminus of EFR3A. Unexpectedly, the C-
85 terminus of EFR3A forms an extended helical interface toward both TTC7B and
86 FAM126A. This interface was validated by both HDX-MS and mutational analysis. The
87 development of a live-cell bioluminescence resonance-energy transfer (BRET)-based
88 assay of PI4KA recruitment to the PM as well as confocal imaging show the key functional
89 role of the EFR3 C-terminus in membrane recruitment of the PI4KA complex. Overall, our

90 findings provide useful insight into the molecular and structural basis of PI4KA regulation
91 at the PM.
92
93 **Results**
94 *Cryo-EM analysis of the EFR3A-PI4KA complex*
95 Investigation into the molecular basis of how EFR3A regulates PI4KA required the
96 production of a stable PI4KA-TTC7B-FAM126A complex. This was achieved by co-
97 expression of full-length PI4KA and TTC7B, together with a truncated FAM126A lacking
98 the disordered C-terminus (1-308, FAM126A ΔC) (**Fig. 1A**). This complex has been
99 structurally characterized (*18*), is homogenous, and elutes off gel filtration consistent with
100 the formation of a dimer of heterotrimers. For simplicity, this complex will be referred to
101 as the PI4KA complex throughout the manuscript. It has previously been established that
102 in yeast the disordered C-terminus of EFR3 mediates recruitment of the TTC7 ortholog
103 Ypp1 (*25*). To identify the related site in human EFR3A we carried out a bioinformatic
104 analysis of sequence conservation. While there were no regions that were strictly
105 conserved between yeast and humans (**Supplemental Fig 1)**, there was a region that
106 was highly conserved among chordates in the C-terminus. We generated multiple
107 constructs spanning this region for expression in *E. coli*, with the most stable and
108 homogenous being a construct spanning residues 721-791 of EFR3A (**Fig. 1A**).
109 To validate that this EFR3A fragment could interact with the PI4KA complex, size
110 exclusion chromatography was used to determine whether complex formation would
111 occur. When co-incubated together, the PI4KA complex co-eluted with the EFR3A C-
112 terminal fragment, with elution volume and SDS-PAGE analysis consistent with a dimer
113 of hetero-tetramers (**Fig. 1B**). We then carried out cryo-EM analysis of this reconstituted
114 complex. While the protein specimen appeared homogeneous on negative stain EM
115 grids, vitrification of this protein product yielded aggregated particles at the air-water
116 interface. To address this problem, we subjected the complex to limited BS^3
117 (bis(sulfosuccinimidyl)suberate) chemical crosslinking followed by size exclusion
118 chromatography, with this complex eluting at a volume similar to the non-crosslinked
119 complex.

120 Using this sample, we were able to generate a cryo-EM reconstruction of the
121 PI4KA complex bound to the C-terminus of EFR3A at a nominal resolution of 3.48Å from
122 67,563 particles (**Fig. 1C, Supplemental Fig 2**). Refinement yielded large differences in
123 local resolution between the two hetero-tetramers. We will therefore focus our
124 descriptions on the better-resolved hetero-tetramer within the assembly. (**Supplemental**
125 **Fig 2C**). Unexpectedly, our structure showed that the EFR3A C-terminus binds to both
126 TTC7B and FAM126A, forming a V-shape composed of three alpha helices. The local
127 resolution of the first interfacial α-helix in EFR3A spanning residues 728-735 was
128 sufficient for unambiguous manual model building into density (**Supplemental Fig 3**). The
129 local resolution of the 2nd and 3rd helices of EFR3A was insufficient for reliable manual
130 model building, so we used rigid body refinement of an AlphaFold3 prediction (*27*, *28*) to
131 model these helices (**Supplemental Fig 3**). Overall, we were able to build a molecular
132 model of residues 724-787 of EFR3A bound to TTC7B-FAM126A (**Fig. 1D**). No direct
133 interactions were seen between the EFR3A C-terminus and PI4KA, with no major
134 conformational changes in the PI4KA subunit. The interface between EFR3A and
135 FAM126A was unexpected, as both EFR3 and TTC7 are conserved from yeast to
136 humans, while FAM126 is conserved only in metazoans (*20*).
137
138 *HDX-MS analysis of the EFR3A-PI4KA complex*
139 To further understand the dynamics of the interaction between the PI4KA complex
140 and EFR3A, we employed HDX-MS, a powerful technique to investigate protein
141 conformational dynamics (*29–31*). HDX-MS experiments were performed on the PI4KA
142 complex with and without EFR3A. Deuterium incorporation was measured over a range
143 of time points (30s, 300s, 3000s, 10000s) and the mass shift upon deuterium
144 incorporation were analysed via mass spectrometry, with significant differences in
145 exchange being defined as changes greater than >0.45 Da and >5% at any time point
146 with unpaired t-test values of $p<0.01$.
147 Multiple regions in both TTC7B and FAM126A showed significant decreases in
148 exchange upon binding to EFR3A. These regions included residues 89-102 in FAM126A
149 and residues 539-544 in TTC7B (**Fig. 2A+B, Supplemental Fig 4**), which were all

150 localized at the interface observed by cryo-EM. No significant changes in exchange were
151 observed in PI4KA, consistent with the lack of direct contacts observed in the cryo-EM
152 structure.

153 Together, the cryo-EM and HDX-MS data suggested that EFR3A would bind
154 similarly to an isolated dimer of TTC7B-FAM126A ΔC. We purified TTC7B-FAM126A ΔC,
155 which will be referred to as TTC7B-FAM126A, from *E. coli*, with gel filtration profiles in the
156 presence of the C-terminus of EFR3A consistent with the formation of a stable trimer (**Fig.**
157 **2C**). To investigate the implications of the lack of PI4KA on conformational dynamics, we
158 used HDX-MS to compare TTC7B-FAM126A in the presence and absence of the C-
159 terminus of EFR3A. HDX-MS experiments were measured over 5 time points (3s, 30s,
160 300s, 3000s and 10,000s at 18°C). We observed significant decreases in HDX in the
161 same sites on TTC7B and FAM126A as observed in the PI4KA complex, with additional
162 regions spanning the entire EFR3A interface, as well as some allosteric differences
163 distant from the EFR3A binding site (**Fig. 2D-E, Supplemental Fig 4**). To map changes
164 in deuterium incorporation in EFR3A, we used a different EFR3A C-terminus construct
165 containing residues 721-791 of EFR3A with an N-terminal maltose binding protein (MBP)
166 tag, with HDX-MS experiments performed on MBP-EFR3A apo and in complex with
167 TTC7B-FAM126A. Deuterium incorporation was measured over 4 time points (3s, 30s,
168 300s at 18°C and 3s at 0°C). Peptides spanning all three helices in EFR3A showed a
169 significant decrease in HDX, further validating the interface observed in the cryo-EM
170 structure (**Fig. 2F-G, Supplemental Fig 4**). We carried out biolayer interferometry (BLI)
171 measurements of TTC7B-FAM126A binding to the C-terminus of EFR3A, with this
172 interface having a K_D of ~63 ± 13 nM (**Fig. 3A**).

173

174 *Molecular details of the EFR3A interface with TTC7B*

175 Our cryo-EM structure revealed that EFR3A engages TTC7B and FAM126A in an
176 extended interface composed of three α-helices from EFR3A oriented in a V, resulting in
177 a buried surface area of ~1500 Å^2. This interface is primarily hydrophobic, with the
178 interface between EFR3A and TTC7B being ~800 Å^2 and consists of the first EFR3A α-
179 helix (residues 728-735) and the latter half of the 3rd EFR3A α-helix (761-785) (**Fig. 3B-**

180 **C**). The first α-helix is likely the most stable as this is the only region of EFR3A visible in
181 both halves of the cryo-EM map and is also the region with the highest local resolution in
182 the electron density (**Fig 2C)**. The α1-helix in EFR3A is amphipathic, with the hydrophobic
183 face primarily interacting with hydrophobic residues in three helices in TTC7B (residues
184 599-616, 690-707, and 712-723). The interacting residues in the α1 and α3 helices of
185 EFR3A are strongly conserved throughout evolution in vertebrates, with partial
186 conservation in metazoans, and very limited conservation in yeast (**Fig 3B and**
187 **Supplemental Fig 1**). There are some notable differences in interfacial residues between
188 EFR3A and EFR3B that may alter binding affinity, potentially highlighting isoform-specific
189 regulatory differences.

190 We generated several point mutations on both EFR3A and TTC7B and used Bio-
191 Layer Interferometry (BLI) to determine their effect on complex formation (**Fig 3F-G and**
192 **Supplemental Fig 5**). Mutation of residues in the α1 helix in EFR3A, including F728A,
193 L731A, K732E, and A734R led to decreased binding, with the L731A mutation causing
194 the largest disruption. Mutation of a corresponding residue in TTC7B (A702R) also led to
195 an almost complete disruption of EFR3A binding, with removal of hydrophobic residues
196 showing a minimal effect on binding affinity. Mutations of residues in the α3 helix of
197 EFR3A, or corresponding residues in TTC7B showed no significant effect on binding,
198 highlighting that the α1 helix of EFR3A is indispensable for binding, with a limited role of
199 the C-terminal half of the α3 helix in EFR3A.

200

201 *Molecular details of the EFR3A interface with FAM126A*

202 It was unexpected that there would be an extensive interface between EFR3A and
203 FAM126A, as FAM126A has not been previously annotated as a critical partner in EFR3-
204 mediated PM recruitment of PI4KA. There is an extended evolutionarily conserved
205 interface between EFR3A and FAM126A (**Fig. 4A-C**). This interface in EFR3A is
206 composed of the C-terminal region of the α2-helix, the N-terminal region of the α3-helix,
207 and the residues between these two helices. This packs up against two α-helices in
208 FAM126A (53-66 and 97-117).

209 We generated several point mutations at the EFR3A-FAM126A interface and used
210 BLI to determine their effect on complex formation (**Fig 4D-E and Supplemental Fig 5**).
211 Mutation of residues F755A and I763A localized at the interface of helix α2 and α3 led to
212 decreased binding, with the F755A mutation causing the largest disruption. Mutation of
213 corresponding residues in FAM126A (F61A and A103R) also led to significant disruption
214 of EFR3A binding. This validates the previously unidentified critical role of FAM126A in
215 EFR3A binding, with this likely having important implications for PI4KA regulation.
216
217 *BRET analysis of EFR3-mediated plasma membrane recruitment*
218 To define the functional role of the identified interface between EFR3 and TTC7-
219 FAM126 in mediating PM localization of PI4KA, we developed a unique bioluminescence
220 resonance energy transfer (BRET) assay. These quantitative measurements used a
221 single-plasmid design containing a PM (Lyn Kinase N-Terminus; L10)-anchored BRET
222 acceptor (mVenus) and a nano-Luciferase (nLuc)-tagged PI4KA, which were separated
223 by a self-cleaving tandem viral 2A peptide sequence (tPT2A) to produce each protein in
224 transfected cells at a fixed stoichiometry (**Fig. 5A**). Upon addition of a cell-permeable
225 luciferase substrate (coelenterazine h; final concentration 5 μM), the signal from the nLuc-
226 generated luminescence and resulting mVenus fluorescence can be measured in entire
227 populations of live cells using a multimode microplate reader. Experiments were carried
228 out by transfecting this PM-PI4KA^{BRET} biosensor (L10-mVenus-tPT2A-nLuc-PI4KA) along
229 with a single-plasmid encoding full length epitope-tagged EFR3B, TTC7B, and FAM126A
230 which also contains unique P2A and T2A splitting sequences between the specific
231 components (EFR3B-P2A-TTC7B-T2A-FAM126A), as we have previously described
232 (*32*).
233 Live-cell experiments were carried out using HEK293A cells expressing a fixed
234 amount of the PM-PI4KA^{BRET} biosensor (500ng/well), along with increasing amounts
235 (100, 500, and 1000 ng/well) of the EFR3B-TTC7B-FAM126A plasmid. Importantly, we
236 saw a clear dose-dependent increase in the basal BRET signal when full-length EFR3B,
237 TTC7B and FAM126A were co-expressed (red bars), consistent with an increase to the
238 PM recruitment of PI4KA (**Fig. 5B**). We performed a control experiment where the C-

239 terminus of EFR3B was truncated (EFR3B Δc-term, where residues 716-817 were
240 truncated) and saw no significant increase in the BRET signal (blue bars) over an empty-
241 vector control (black bars). This is consistent with the C-terminus of EFR3 being required
242 for EFR3 mediated PM recruitment of PI4KA. Subsequently, we incorporated complex
243 disrupting mutations in EFR3B (L726A, F751A; green bars), TTC7B (A702R; grey bars),
244 or FAM126A (A103R; magenta bars), and saw a significantly reduced BRET signal across
245 the various levels of relative plasmid expression when compared to the wild-type controls.
246 However, all these mutants still had a measurable BRET signal above that of the
247 truncated EFR3B control (**Fig. 5B**). This indicates the importance of avidity in PI4KA
248 recruitment, as none of these mutations affecting the complex interface were able to
249 completely abrogate PI4KA localization to the PM. In parallel with this BRET-based
250 approach, we also used confocal microscopy for live-cell imaging studies to examine the
251 subcellular localization of an EGFP-tagged PI4KA construct after co-expression of
252 EFR3B, TTC7B, and FAM126A. Similar to our quantitative BRET-based measurements,
253 we only saw robust PM localization of EGFP-PI4KA when co-expressed together with the
254 wild-type EFR3B, TTC7B and FAM126A, and very limited PM localization of EGFP-PI4KA
255 in conjunction with the mutant or truncated versions of EFR3B, TTC7B, and FAM126A
256 (**Fig. 5C**).
257

258 **Discussion**

259 Understanding how PI4KA is recruited, activated, and regulated at the PM is
260 essential in developing therapeutic strategies for targeting human diseases associated
261 with loss-of-function of PI4KA. PI4KA, TTC7A and FAM126A mutations have been
262 identified in immunological, neurological, gastrointestinal, and developmental disorders
263 (*9–12*, *19*, *33*). Some cancers also require EFR3 and PI4KA activity for their aggressive
264 growth (*14*, *15*). Here, we report the architecture of the EFR3A complex that is formed
265 with PI4KA-TTC7B-FAM126A, revealing novel insights into the molecular mechanisms
266 underlying PM recruitment of PI4KA.

267 Our cryo-EM and HDX-MS analyses reveal that EFR3A forms an extended
268 interface with both the TTC7 and FAM126 regulatory proteins. Previous analysis of

evolutionarily conserved surfaces in TTC7 and FAM126 had led to the proposal of an EFR3 interface composed of both proteins (*18*), and our work provides the first experimental evidence of the cooperation between TTC7 and FAM126 for EFR3 binding. This was validated by complex-disrupting mutations in EFR3A at both the FAM126A and TTC7B interfaces, as well as mutations in FAM126A and TTC7B at the interface with EFR3A. There was no difference in the conformation of PI4KA upon binding EFR3A in solution, suggesting that there are no allosteric conformational changes upon EFR3A binding. However, further biochemical and biophysical analysis of membrane resident full-length EFR3 recruiting the PI4KA complex to membranes will be required to fully understand the conformational dynamics of PI4KA upon membrane recruitment.

An important implication of this structure is that the two EFR3 isoforms may be able to be selectively recruited to specific combinations of TTC7 and FAM126 isoforms. While the binding interfaces are conserved in different isoforms, this conservation is not absolute, allowing for the possibility of unique binding affinities. TTC7A has a 50% sequence similarity with TTC7B, while FAM126A has a 54% sequence similarity to FAM126B. Some of the most conserved regions are located at the EFR3 interface. For EFR3, the C-terminus has a 67% sequence similarity between EFR3A and EFR3B, with most of the interfacial residues being strongly conserved. It is still not known if these sequence differences drive different roles of TTC7/FAM126/EFR3 isoforms or if these differences are due to variable tissue expression. Isoforms of TTC7, FAM126 and EFR3 are differentially expressed in diverse tissues, with many tissues expressing multiple isoforms. The isoform-specific roles of the PI4KA regulatory proteins are still not fully elucidated.

The potential for unique molecular roles for the isoform-specific PI4KA complexes has been recently highlighted for TTC7A and TTC7B, with patients having disease-linked loss of function mutations in TTC7A in tissues that express both TTC7A and TTC7B, where it appears that TTC7B cannot compensate for the loss of TTC7A. This may be driven by differences in TTC7A/TTC7B expression during embryogenesis, where TTC7A is widely expressed, and TTC7B is primarily expressed in brain tissues (*34*). As the experimental structure of TTC7A is unknown, we examined AlphaFold3 predicted models

299 of TTC7A compared to our structure, with a focus on potential differences at the EFR3A
300 interface. Intriguingly, there is a weakly predicted TTC7A helix (residues 678-690) in the
301 same location as the α1 helix of EFR3A, with this region being only weakly conserved in
302 TTC7B (**Supplemental Fig 6A**) (*35*). In both TTC7A and TTC7B there are multiple
303 putative phosphorylated residues in this region (*36*), which may alter the conformation of
304 the EFR3 binding surface. Further analysis of differences in EFR3 binding to TTC7A or
305 TTC7B containing PI4KA complexes and how phosphorylation of TTC7A/B alters EFR3
306 binding will be required to understand the dynamic regulation of PI4KA membrane
307 recruitment.

308 EFR3 proteins act as the membrane localization signal for the PI4KA complex (*5*),
309 with a palmitoylation code controlling their spatial organisation between liquid-ordered
310 and disordered regions of the PM (*23*). It has been previously revealed that there is an
311 aspect of plasticity in how EFR3 recruits PI4KA, as the integral membrane protein
312 TMEM150A can function in tandem with EFR3 to recruit PI4KA to the PM in the absence
313 of TTC7-FAM126 (*23*, *37*). Our structure reveals the canonical mechanism of PM
314 recruitment mediated by TTC7-FAM126. EFR3A mutations developed in this study that
315 disrupt only TTC7-FAM126-mediated recruitment may also act as unique tools to discern
316 between the diverse mechanisms of PI4KA recruitment to the PM. The triple helical
317 binding interface of EFR3 that binds to TTC7-FAM126 contains multiple phosphorylation
318 sites, present in both EFR3A and EFR3B (*36*). The location of these sites is divergent
319 between EFR3A and EFR3B, potentially suggesting differential regulation
320 (**Supplemental Fig 6B**). Intriguingly, the interfacial F728 in EFR3A is not conserved in
321 EFR3B, with this residue being Y723 in EFR3B. This residue can be phosphorylated, with
322 this PTM likely to dramatically decrease binding due to disruption of the TTC7-EFR3B
323 interface. Further identification of the kinases and phosphatases that target these sites
324 will be required to fully understand how the EFR3 interface can be regulated.

325 While subtle differences between complexes of TTC7A and TTC7B with the EFR3
326 C-terminus and FAM126 may exist, our structure of EFR3A bound to PI4KA-TTC7B-
327 FAM126A still allows for interrogation of the possible molecular mechanisms underlying
328 missense, nonsense and point mutations in TTC7A that cause severe gastrointestinal

329 and immunological disease. This disease is an autosomal-recessive inherited disease,
330 with patients having heterogeneous intestinal and immunologic disease presentations.
331 The most severe TTC7A mutations cause nonsense or frameshift mutations in TTC7A
332 that collectively remove both the EFR3 and PI4KA binding sites (*34*). However, there are
333 numerous missense mutations that cluster to regions in spatial proximity to the putative
334 EFR3 binding site in TTC7A. The mutations S539L, A551D, and H570R are all in helices
335 that either bind the α3 helix of EFR3A, or pack against the interfacial helices, with these
336 likely altering the orientation of the EFR3A binding site. In addition, K606R is predicted to
337 pack against the helix 704-724 in TTC7A (equivalent to the EFR3 interfacial helix 690-
338 707 in TTC7B). This mutation would likely alter the orientation of the EFR3 interface,
339 causing decreased affinity. Further biochemical and biophysical analysis will be required
340 to define the effect of disease-causing TTC7A mutations on EFR3-mediated membrane
341 recruitment versus PI4KA complex stability.

342 A limitation of the molecular insight we have observed for how EFR3 interacts with
343 the PI4KA complex is that all our biophysical observations on the association of the EFR3
344 C-terminus with the PI4KA complex were carried out exclusively in solution. The
345 biologically relevant association of EFR3 will occur in the context of the full length EFR3
346 localised on a membrane surface. While we have no expectation of the ordered domains
347 of EFR3 altering how the C-terminus binds to the PI4KA complex, there likely will be a
348 critical role of this region in proper EFR3 membrane localisation. For the evolutionarily
349 similar class I-III PI3Ks and PI4KB there are extensive conformational changes in the lipid
350 kinase domain that are driven by association with membrane substrate, and it is likely
351 that this will also be the case for PI4KA. To completely identify the full repertoire of
352 regulatory mechanisms underlying PI4KA activation future experiments will need to
353 address conformational dynamics of full-length lipidated EFR3 recruitment of the PI4KA
354 complex in its native membrane environment.

355 Collectively, our detailed biochemical and structural analyses of the EFR3A-
356 mediated recruitment of PI4KA complex to the PM provides unique insight into the
357 assembly and regulation of PI4KA complexes. This work also provides a framework to
358 further explore how PM recruitment of PI4KA is regulated. Overall, the findings from this

study will be useful in developing novel therapeutic strategies to target aberrant PI4KA signaling in human disease.

Acknowledgements

JEB is supported by the Canadian Institute of Health Research, and a Michael Smith Foundation for Health Research (Scholar Award 17686). ALS was supported by an NSERC CGS-M scholarship. C.K.Y. is supported by CIHR (PJT-168907) and the Natural Sciences and Engineering Research Council of Canada (RGPIN-2018-03951). Cryo-EM specimens were prepared, and data was collected at the High-Resolution Macromolecular Electron Microscopy (HRMEM) facility at the University of British Columbia (https://cryoem.med.ubc.ca). We thank Claire Atkinson, Joeseph Felt, Liam Worrall and Natalie Strynadka. HRMEM is funded by the Canadian Foundation for Innovation and the British Columbia Knowledge Development Fund. The work of TB, JGP, PR and AAP was funded by the Intramural Research Program of the *Eunice Kennedy Shriver* National Institute of Child Health and Human Development of the National Institutes of Health, Bethesda, MD, USA. (HHS/NIH/NICHD - Z01:HD000196-25). Confocal imaging was performed at the Microscopy & Imaging Core of the NICHD with the kind assistance of Drs. Vincent Schram and Ling Yi.

Competing Interests

J.E.B. reports personal fees from Scorpion Therapeutics and Reactive therapeutics; and research contracts from Novartis and Calico Life Sciences.

Data Availability

The EM data have been deposited in the EM data bank with accession number (EMDB: 44413), and the associated structural model has been deposited to the PDB with accession number (PDB: 9BAX). The MS proteomics data have been deposited to the ProteomeXchange Consortium via the PRIDE partner repository with the dataset identifier PXD043442 (*38*). All raw data in all figures are available in the source data excel file.

389 **Methods**

390 ***Plasmid constructs***

391 Plasmids containing genes for full length PI4KA, TTC7B and FAM126A (1-308) were
392 cloned into the MultiBac vector, pACEBac1 (Geneva Biotech) as described in (*21*).
393 Plasmid encoding TTC7B and FAM126A (1-308) was subcloned into a pOPT vector
394 containing an N-terminal 10X histidine tag, followed by a 2X Strep tag, followed by a
395 Tobacco Etch Virus (TEV) protease cleavage site. Based on the evolutionary
396 conservation of the C-terminal tail of EFR3A (**Fig. S1**), we designed and synthesized a
397 construct containing the C-terminus of EFR3A from residue 688 to 821 from GeneArt
398 gene synthesis (Invitrogen). EFR3A (721-791) was subcloned into two pOPT vectors; one
399 containing an N-terminal 10X histidine tag and a 2X Strep tag, and one containing an N
400 terminal Maltose Binding Protein (MBP) tag in addition to the 10X Histidine tag and 2X
401 Strep tag (*39*). EFR3A, TTC7B and FAM126A substitution mutants shown in Table S2
402 were generated using site-directed mutagenesis according to published protocols using
403 EFR3A (721-791) as template. Plasmid encoding human EFR3B^{HA}-T2A-TTCB^{MYC}-P2A-
404 ^{FLAG}FAM126A in pcDNA3.1 vector, which is referred to more simply here as EFR3B-P2A-
405 TTC7B-T2A-FAM126A was a kind gift from the Cyert lab at Stanford university. EFR3B,
406 TTC7B and FAM126A substitution and deletion mutants shown in Table S2 in the
407 pcDNA3.1 vector were generated using Gibson assembly (*39*).

408 Alternatively, the high-sensitivity PM-PI4KA^{BRET} biosensor (L10-mVenus-tPT2A-
409 nLuc-PI4KA) was constructed in multiple steps by standard restriction cloning using
410 enzymes from New England Biolabs. First, the sLuc cassette in the L10-mVenus-T2A-
411 sLuc-(2X)P4M biosensor (*40*) was exchanged for NanoLuciferase (nLuc) using an insert
412 amplified from PM-nLuc (Forward Primer, 5'- AT ATA CCG GTC ATG GTC TTC ACA
413 CTC GAA GAT TTC GTT GG -3'; Reverse Primer, 5'- AT ATC TCG AGA CGC CAG AAT
414 GCG TTC GCA CAG C -3'), which was a kind gift from Laszlo Hunyady (Addgene Plasmid
415 # 164784), together with AgeI and XhoI restriction sites. Next, we replaced the single T2A
416 site in the resulting L10-mVenus-T2A-nLuc-(2X)P4M biosensor with the tandem tPT2A
417 sequence (*41*) using a custom-synthesized insert from GeneArt (Invitrogen) and a SalI
418 and AgeI double-digest. Finally, we replaced the (2X)P4M domain in the L10-mVenus-

419 tPT2A-nLuc-(2X)P4M vector with an in-frame PI4KA insert derived from pEGFP-PI4KA
420 (*42*) using shared XhoI and MfeI restriction sites in the parent C1 vector backbones
421 (CloneTech). Whole plasmid sequencing for all plasmids was performed by
422 Plasmidsaurus using Oxford Nanopore Technology with custom analysis and annotation.
423

424 ***Protein Expression***

425 Plasmids containing the coding sequences for EFR3A (721-791), EFR3A mutants and
426 MBP-EFR3A (721-791) were expressed in BL21 DE3 C41 *Escherichia coli* and induced
427 with 0.5 mM IPTG and grown at 37 °C for 4 h. The TTC7B-FAM126A (1-308) construct
428 was expressed in BL21 DE3 C41 cells and induced with 0.1mM IPTG and grown at 21
429 °C for 20 hours. Cells were then harvested and centrifuged at 15,000*g*. Pellets were
430 washed with PBS before being snap-frozen in liquid nitrogen, followed by storage at –80
431 °C. Bacmid harboring PI4KA complex (PI4KA-TTC7B-FAM126A (1-308)) was transfected
432 into *Spodoptera frugiperda (Sf9) cells*, and viral stocks amplified for one generation to
433 acquire a P2 generation final viral stock. Final viral stocks were added to *Sf9* cells in a
434 1/100 virus volume to cell volume ratio. Constructs were expressed for 65-72 hours before
435 harvesting of the infected cells. Cell pellets were washed with PBS, flash frozen in liquid
436 nitrogen, and stored at –80 °C.
437

438 ***Protein Purification***

439 *EFR3A, EFR3A mutants and MBP-EFR3A purification:* Cell pellets were lysed by
440 sonication for 5 min in lysis buffer (20 mM Tris [pH 8.0], 100 mM NaCl, 5% [v/v] glycerol,
441 20 mM imidazole, 2 mM β-mercaptoethanol [bME]), and protease inhibitors [Millipore
442 Protease Inhibitor Cocktail Set III, EDTA free]). Triton X-100 was added to 0.1% v/v, and
443 the solution was centrifuged for 45 min at 20,000*g* at 1 °C (Beckman Coulter J2-21, JA-
444 20 rotor). The supernatant was then loaded onto a 5 ml HisTrap column (Cytiva) that had
445 been equilibrated in nickel–nitrilotriacetic acid (Ni–NTA) A buffer (20 mM Tris [pH 8.0],
446 100 mM NaCl, 20 mM imidazole [pH 8.0], 5% [v/v] glycerol, and 2 mM bME). The column
447 was washed with of high salt buffer (20 mM Tris [pH 8.0], 1 M NaCl, 5% [v/v] glycerol,
448 and 2 mM bME), followed by of 6% Ni–NTA B buffer (20 mM Tris [pH 8.0], 100 mM NaCl,

449 200 mM imidazole [pH 8.0], 5% [v/v] glycerol, and 2 mM bME) before being eluted with
450 100% Ni–NTA B. The eluate was then loaded onto a 5 ml Strep column and then washed
451 with GFB (20 mM HEPES [pH 7.5], 150 mM NaCl, 5% [v/v] glycerol and 1 mM Tris(2-
452 carboxyethyl) phosphine [TCEP]). Protein was eluted with GFB containing 2.5 mM
453 desthiobiotin and concentrated in a 10 kDa MWCO concentrator (Millipore Sigma).
454 Concentrated protein was loaded onto the Superdex 75 Increase 10/300 GL (Cytiva) or
455 the Superdex 200 Increase 10/300 GL (Cytiva) pre-equilibrated in GFB. Protein fractions
456 were collected and concentrated in a 10 kDa MWCO concentrator (Millipore Sigma), flash
457 frozen in liquid nitrogen, and stored at –80 °C.

458 *TTC7B-FAM126A (1-308) purification:* Cell pellets were lysed by sonication for
459 5 min in lysis buffer (20 mM imidazole [pH 8.0], 100 mM NaCl, 5% [v/v] glycerol, 2 mM
460 bME), and protease inhibitors [Millipore Protease Inhibitor Cocktail Set III, animal-free].
461 Triton X-100 was added to 0.1% v/v, and the solution was centrifuged for 45 min at
462 20,000*g* at 1 °C. The supernatant was then loaded onto a 5 ml HisTrap column (Cytiva)
463 that had been equilibrated in nickel–nitrilotriacetic acid (Ni–NTA) A buffer (20 mM Tris [pH
464 8.0], 100 mM NaCl, 20 mM imidazole [pH 8.0], 5% [v/v] glycerol, and 2 mM bME). The
465 column was washed with Ni-NTA A buffer (20 mM imidazole [pH 8.0], 100 mM NaCl, 5%
466 [v/v] glycerol, and 2 mM bME) followed by 6% Ni–NTA B buffer (450 mM Imidazole [pH
467 8.0], 100 mM NaCl, 5% [v/v] glycerol, and 2 mM bME) before being eluted with 100% Ni–
468 NTA B. The eluate was then loaded onto a 5 ml Strep column and then washed with
469 filtration buffer (GFB) (20 mM Imidazole [pH 7.0], 150 mM NaCl, 5% [v/v] glycerol and
470 0.5 mM Tris(2-carboxyethyl) phosphine (TCEP)). The column was loaded with tobacco
471 etch virus protease containing a stabilizing lipoyl domain. TEV cleavage proceeded
472 overnight following which the protein was eluted with GFB. Protein eluate was further
473 concentrated in a 50 kDa MWCO concentrator (Millipore Sigma). Concentrated protein
474 was loaded onto the Superdex 200 Increase 10/300 GL (Cytiva) or the Superose 6
475 Increase 10/300 GL (Cytiva) pre-equilibrated in GFB. Protein fractions from a single peak
476 were collected and concentrated in 50 kDa MWCO concentrator (Millipore Sigma), flash
477 frozen in liquid nitrogen and stored at -80 °C until further use. This protein is referred to
478 as TTC7B-FAM126A.

479 *PI4KA-TTC7B-FAM126A (1-308) purification*: Sf9 pellets were resuspended in
480 lysis buffer [20 mM imidazole pH 8.0, 100 mM NaCl, 5% glycerol, 2 mM βMe, protease
481 (Protease Inhibitor Cocktail Set III, Sigma)] and lysed by sonication. Triton X-100 was
482 added to 0.1% v/v final, and lysate was centrifuged for 45 min at 20,000×g at 1 °C. The
483 supernatant was then loaded onto a 5 ml HisTrap column (Cytiva) that had been
484 equilibrated in nickel–nitrilotriacetic acid (Ni–NTA) A buffer (20 mM Tris [pH 8.0], 100 mM
485 NaCl, 20 mM imidazole [pH 8.0], 5% [v/v] glycerol, and 2 mM bME). The column was
486 washed with Ni-NTA A buffer (20 mM imidazole [pH 8.0], 100 mM NaCl, 5% [v/v] glycerol,
487 and 2 mM bME) followed by 6% Ni–NTA B buffer (27 mM Imidazole [pH 8.0], 100 mM
488 NaCl, 5% [v/v] glycerol, and 2 mM bME) before being eluted with 100% Ni–NTA B. Elution
489 fractions were passed through a 5 ml StrepTrapHP column (Cytiva) pre-equilibrated in
490 Gel Filtration buffer (GFB) (20 mM imidazole pH 7.0, 150 mM NaCl, 5% glycerol [v/v], 0.5
491 mM TCEP). The column was washed with GFB before loading a tobacco etch virus
492 protease containing a stabilizing lipoyl domain (Lip-TEV), and cleavage proceeded
493 overnight. Cleaved protein was eluted with GFB and concentrated in a 50 kDa MWCO
494 concentrator (MilliporeSigma). Concentrated protein was loaded onto the Superose 6
495 Increase 10/300 GL (Cytiva) pre-equilibrated in GFB. Protein fractions from a single peak
496 were collected and concentrated in 50 kDa MWCO concentrator (Millipore Sigma), flash-
497 frozen in liquid nitrogen and stored at -80 °C until further use. This protein is referred to
498 as PI4KA complex.
499 The raw SDS-PAGE gel images for all purified proteins after gel filtration are shown
500 in the source data.
501
502 ***Co-elution of PI4KA complex-EFR3A and TTC7B-FAM126A (1-308)-EFR3A***
503 7.19 μM of PI4KA complex and 61.8 μM of EFR3A were loaded onto a Superose 6
504 Increase column pre-equilibrated in GFB [150 mM NaCl, 20 mM imidazole (pH 7.0), 5%
505 glycerol (v/v), 0.5 mM TCEP]. Fractions containing the PI4KA complex bound to EFR3A
506 were pooled, concentrated, flash-frozen in liquid nitrogen and stored at -80°C. Protein
507 was run on an SDS-PAGE gel to confirm the formation of the complex. For the co-elution
508 of TTC7B-FAM126A (1-308) and EFR3A, we used 6.78 μM of TTC7B-FAM126A and

509 102.3 µM of EFR3A and performed size exclusion chromatography as mentioned above.
510 The peaks were run on a SDS-PAGE gel to confirm formation of the complex.
511
512 ***Protein purification for Cryo-EM***
513 Pre-Gel filtered PI4KA complex (13.0 µM final), and gel filtered EFR3A (113 µM final)
514 were incubated together on ice for 20 minutes prior to injection onto the Superose 6
515 Increase 10/300 GL (Cytiva) pre-equilibrated in GFB (150 mM NaCl, 20 mM imidazole
516 [pH 7.0], 5% glycerol [v/v], 0.5 mM TCEP). Protein fractions from a single peak were
517 collected and concentrated to 250 µl at 4µM and BS3 was added to a final concentration
518 of 1 mM. The reaction was incubated on ice for 1 hour. 1 M Tris (pH 7.5) was added to a
519 final concentration of 50 mM to quench the reaction and incubated at RT for 15 minutes.
520 The quenched reaction was loaded onto the Superose 6 Increase 10/300 column pre-
521 equilibrated in GFB. Protein fractions from the main peak, consistent with an elution
522 volume of the PI4KA complex-EFR3A (721-791), were collected, concentrated, flash
523 frozen in liquid nitrogen, and stored at -80°C.
524
525 ***Cryo-EM sample preparation and data collection***
526 C-Flat 2/1-3Cu-T-50 grids mesh grids were glow-discharged for 25 s at 15 mA using a
527 Pelco easiGlow glow discharger. 3 µL of crosslinked PI4KA complex-EFR3A (721-791)
528 were applied to the grids at 0.7 mg/ml. The grids were prepared using a Vitrobot Mark IV
529 (FEI) by blotting for 1.5 seconds at a blot force of -5 at 4°C and 100% humidity before
530 plunge freezing in liquid ethane. Grids were screened for particle and ice quality at the
531 UBC High Resolution Macromolecular Cryo-Electron Microscopy (HRMEM) facility using
532 a 200-kV Glacios transmission microscope (Thermo Fisher Scientific) equipped with a
533 Falcon 3EC direct electron detector (DED). Datasets were collected at the UBC HRMEM
534 facility using a 300-kV Titan Krios equipped with Selectris energy filter with a Falcon IV
535 camera. A total of 9,412 super-resolution movies were collected using SerialEM with a
536 total dose of 50 e^{-}/Å^{2} over 774 frames at a physical pixel size of 0.77 Å per pixel, using a
537 defocus range of -0.5 to -2 um, at 165,000 x magnification.
538

539 ***Cryo-EM image processing***

540 All data processing was carried out with cryoSPARC v4.2.1. Patch motion correction
541 using default settings was applied to all movies to align the frames and Fourier-crop the
542 outputs by a factor of 2. The contrast transfer function (CTF) of the resulting micrographs
543 was estimated using the patch CTF estimation job with default settings. Micrographs were
544 manually curated to contain micrographs with CTF fit resolution less than or equal to 10.

545 To generate an initial model, 277,573 particles were picked from 3,501
546 micrographs using blob picking with a minimum and maximum diameter of 250 and 280,
547 respectively. Particles were inspected using the inspect picks job to remove particles that
548 picked ice contamination and were then extracted with a box size of 500 pixels, for a total
549 of 201,081 particles. The particles were subjected to 2D classification using default
550 settings. The best class averages were then selected and used as an initial model for
551 template picking. These 2D classes were low pass filtered to 20 Å and used to template
552 pick with the particle diameter set to 300 Å. Particles were inspected and 510,887 were
553 extracted with a box size of 600 pixels and subjected to two rounds of 2D classification
554 with 40 online-EM iterations to remove particles with ice contamination or those that
555 showed no features. A total of 77,624 particles were used for ab initio reconstruction and
556 heterogeneous refinement using three classes, with C1 symmetry. Given the previously
557 solved PI4KA/TTC7B/FAM126A (2-289) cryo-EM structure employing C2 symmetry (*18*),
558 the following homogenous refinements were done with C2 symmetry. The best
559 heterogeneous refinement which had 46,039 particles underwent two rounds of
560 homogenous refinement. These 46,039 particles were subjected to further ab initio 3D
561 reconstructions, heterogeneous refinement, and homogeneous refinement jobs to filter
562 out incorrectly assigned particles. The final initial model to be used to generate templates
563 for auto-picking of particles consisted of 8,647 particles.

564 To generate a cryo-EM map from the complete dataset, the collected movies were
565 split into three groups (Group 1: 3,535 movies, Group 2: 3,364 movies, Group 3: 2,513
566 movies) and processed into micrographs as described above. The initial template from
567 above was used to auto-pick 493,392 (group 1), 415,293 (group 2), and 307,632 (group
568 3) particles, using the template picker job with particle diameter set to 300 Å and a

569 minimum separation distance of 0.75 diameters. Particles were inspected as above and
570 275,667 (group 1), 264,196 (group 2), and 185,766 (group 3) particles were extracted
571 with a box size of 600 pixels. Each group of particles independently underwent one (group
572 1) or two (groups 2 and 3) rounds of 2D classification with 40 online-EM iterations. The
573 resulting 105,657 (group 1), 57,805 (group 2), and 77,900 (group 3) particles were
574 independently used for ab initio reconstruction using 3 classes and subsequent
575 heterogeneous refinement with C1 symmetry. The best 3D classification from groups 1
576 and 2 were merged into 93,029 particles (55,802 (group 1) + 37,227 (group 2)) and
577 underwent two rounds of ab initio reconstruction with 3 classes followed by heterogenous
578 refinement. The best 3D classification, consisting of 44,305 particles was refined using
579 homogeneous refinement using C1 symmetry. The particles from group 3 were then
580 added to these 44,305 particles. A total of 67,563 particles were used to carry out
581 homogeneous refinement, followed by masked local refinement with a static mask using
582 the previous 3D reconstruction as the starting model, yielding a reconstruction with an
583 overall resolution of 3.48 Å based on the Fourier shell correlation (FSC) 0.143 criterion.
584 The full workflow to generate the final cryo-EM map from the three groups is shown in
585 **Supplemental Fig 2.**
586
587 **AlphaFold3 modelling**
588 We used the protein prediction software, AlphaFold3 (*43*) to predict where EFR3A's c-
589 terminus interacts with the TTC7B/FAM126A . Specifically, we used the AlphaFold server
590 (https://golgi.sandbox.google.com/) and input the sequence for full length human TTC7B
591 and FAM126A with the C-terminus of human EFR3A (aa 621-821). To evaluate the
592 confidence of individual subunit assembly predictions, we analysed the predicted
593 alignment error (pae), predicted template modelling score (PTM) and the interface
594 predicted template modelling score. The top ranked model had ptm and iptm scores of
595 0.73 and 0.79, respectively, consistent with a stable complex. The chain_pair_iptm scores
596 are useful in evaluating the confidence of predicted protein-protein interfaces. The
597 chain_pair_iptm score for TTC7B:FAM126A was 0.82, TTC7B:EFR3A was 0.63, and
598 FAM126A:EFR3A was 0.35. The chain_pair_pae_min values correlate with whether two

599 chains interact with each other. The chain_pair_pae_min score for TTC7B:FAM126A was
600 1.15, TTC7B:EFR3A was 1.88, and FAM126A:EFR3A was 1.6. These iptm and pae
601 scores are consistent with a high confidence protein complex prediction.
602
603 ***Model building***
604 The cryo-EM structure of PI4KA-TTC7B-FAM126A (PDB: 6BQ1) (*18*) was fit into the map
605 using Chimera(*44*). The 1st helix of EFR3A was at sufficient local resolution for iterative
606 rounds of automated model building in Phenix, manual model building in COOT, and
607 refinement in Phenix.real_space_refine using realspace, rigid body, and adp refinement
608 with tight secondary structure restraints (*45*). For the remainder of the EFR3A interface
609 with FAM126A and TTC7B we used AlphaFold-Multimer using Google Colab
610 (*28*)(https://colab.research.google.com/github/sokrypton/ColabFold/blob/main/AlphaFold
611 2.ipynb) was used to model the structure of TTC7B-FAM126A–EFR3A. The sequences
612 of full length TTC7B, residues 1-360 of FAM126A with residues 681-821 of EFR3A were
613 input to generate the model of the complex. AlphaFold generated five models ranked in
614 order by mean pLDDT. The highest ranked model showed strong correlation to the cryo-
615 EM density, and was used to model the 2nd and 3rd helix of EFR3A bound to FAM126A
616 and TTC7B, with multiple rounds of refinement in Phenix.real_space_refine using
617 realspace, rigid body, and adp refinement with tight secondary structure restraints (*45*).
618 The full refinement and validation statistics are shown in **Supplementary Table 1**.
619
620 ***HDX-MS sample preparation***
621 HDX reactions examining the TTC7B-FAM126A (1-308) in the presence and absence of
622 EFR3A were carried out in 15 μL reaction volumes containing 15 pmol of protein (1 μM
623 TTC7B-FAM126A, 1 μM EFR3A in the bound state). The exchange reactions were
624 initiated by the addition of 12.55 μL of D_2O buffer (20 mM Imidazole pH 7, 150 mM NaCl)
625 to 2.45 μL of protein (final D_2O concentration of 78.2% [v/v]). Reactions proceeded for 3s,
626 30s, 300s, 3000s, and 10,000s at 20°C before being quenched with ice cold acidic quench
627 buffer, resulting in a final concentration of 0.6M guanidine HCl and 0.9% formic acid.

628 HDX reactions examining the PI4KA complex in the presence and absence of
629 EFR3A were carried out in 15 μL reaction volumes containing 10 pmol of protein (0.667
630 μM PI4KA complex, 0.667 μM EFR3A in the bound state). The exchange reactions were
631 initiated by the addition of 10.92 μL of D_2O buffer (20 mM Imidazole pH 7, 150 mM NaCl)
632 to 4.08 μL of protein (final D_2O concentration of 68.0 % [v/v]). Reactions proceeded for
633 30s, 300s, 3000s, and 10,000s at 20°C before being quenched with ice cold acidic quench
634 buffer, resulting in a final concentration of 0.6M guanidine HCl and 0.9% formic acid post
635 quench.
636 HDX reactions examining MBP-EFR3A in the presence and absence of the
637 TTC7B-FAM126A (1-308) were carried out in 20 μL reaction volumes containing 25 pmol
638 of protein (1.25 μM MBP-EFR3A, 1.25 μM TTC7B-FAM126A in the bound state). The
639 exchange reactions were initiated by the addition of 14.66 μL of D_2O buffer (20 mM
640 Imidazole pH 7, 150 mM NaCl) to 5.34 μL of protein (final D_2O concentration of 68.5 %
641 [v/v]). Reactions proceeded for 3s, 30s, and 300s at 20°C and 0.3s (3s on ice) before
642 being quenched with ice cold acidic quench buffer, resulting in a final concentration of
643 0.6M guanidine HCl and 0.9% formic acid post quench.
644 All conditions and timepoints were created and run in independent triplicate. All
645 samples were flash frozen immediately after quenching and stored at -80°C.
646
647 ***Protein digestion and MS/MS data collection***
648 Protein samples were rapidly thawed and injected onto an integrated fluidics system
649 containing a HDx-3 PAL liquid handling robot and climate-controlled (2°C)
650 chromatography system (Trajan), a Dionex Ultimate 3000 UHPLC system, as well as an
651 Impact HD QTOF Mass spectrometer (Bruker). The full details of the automated LC
652 system are described in (*46*). The TTC7B-FAM126A and PI4KA complex samples were
653 run over one immobilized pepsin column (Trajan; ProDx protease column, 2.1 mm x 30
654 mm PDX.PP01-F32) at 200 μL/min for 3 minutes at 10°C, and the MBP-EFR3A samples
655 were run over two immobilized pepsin columns (Waters; Enzymate Protein Pepsin
656 Column, 300Å, 5μm, 2.1 mm X 30 mm) at 350 μL/min for 3 minutes at 2°C. The resulting
657 peptides were collected and desalted on a C18 trap column (Acquity UPLC BEH C18

658 1.7mm column (2.1 mm x 5 mm); Waters 186004629). The trap was subsequently eluted
659 in line with an ACQUITY 1.7 µm particle, 100 mm × 2.1 mm C18 UPLC column (Waters;
660 186003686), using a gradient of 3-35% B (Buffer A 0.1% formic acid; Buffer B 100%
661 acetonitrile) over 11 minutes immediately followed by a gradient of 35-80% over 5
662 minutes. Mass spectrometry experiments acquired over a mass range from 150 to 2200
663 m/z using an electrospray ionization source operated at a temperature of 200°C and a
664 spray voltage of 4.5 kV.
665
666 ***Peptide identification***
667 Peptides were identified from non-deuterated samples using data-dependent acquisition
668 following tandem MS/MS experiments (0.5s precursor scan from 150-2000 m/z; twelve
669 0.25s fragment scans from 150-2000 m/z). TTC7B-FAM126A (1-308) and PI4KA complex
670 MS/MS datasets were analysed using PEAKS7 (PEAKS), and peptide identification was
671 carried out using a false discovery-based approach, with a threshold set to 1% using a
672 database of purified proteins and known contaminants (*47*). The search parameters were
673 set with a precursor tolerance of 20 ppm, fragment mass error 0.02 Da charge states from
674 1-8, leading to a selection criterion of peptides that had a -10logP score of 25.2 and 20.4
675 respectively. MBP-EFR3A (721-791) MS/MS datasets were analysed using FragPipe
676 v18.0 and peptide identification was carried out by using a false discovery-based
677 approach using a database of purified proteins and known contaminants (*47*, *48*).
678 MSFragger was used, and the precursor mass tolerance error was set to -20 to 20ppm.
679 The fragment mass tolerance was set at 20ppm. Protein digestion was set as nonspecific,
680 searching between lengths of 4 and 50 aa, with a mass range of 400 to 5000 Da.
681
682 ***Mass Analysis of Peptide Centroids and Measurement of Deuterium Incorporation***
683 HD-Examiner Software (Sierra Analytics) was used to automatically calculate the level of
684 deuterium incorporation into each peptide. All peptides were manually inspected for
685 correct charge state, correct retention time, appropriate selection of isotopic distribution,
686 etc. Deuteration levels were calculated using the centroid of the experimental isotope
687 clusters. Results are presented as relative levels of deuterium incorporation, and the only

688 control for back exchange was the level of deuterium present in the buffer (78.2%, 68.0%,
689 or 68.5%). Differences in exchange in a peptide were considered significant if they met
690 all three of the following criteria: ≥5% change in exchange, ≥0.45 Da difference in
691 exchange, and a p value <0.01 using a two tailed student t-test. The entire HDX-MS
692 dataset with all the values and statistics are provided in the source data. Samples were
693 only compared within a single experiment and were never compared to experiments
694 completed at a different time with a different final D_2O level. The data analysis statistics
695 for all HDX-MS experiments are provided in the source data according to the guidelines
696 of (*31*). HDX-MS proteomics data generated in this study have been deposited to the
697 ProteomeXchange Consortium via the PRIDE partner repository with the dataset identifier
698 PXD043442 (*38*).
699
700 ***Bio-layer interferometry (BLI)***
701 The BLI measurements were conducted using a Fortebio (Sartorius) K2 Octet
702 using fiber optic biosensors. Anti–penta-His biosensors were loaded using purified MBP-
703 EFR3A, which had a 10x His tag on the N-terminus. The biosensor tips were preincubated
704 in the BLI buffer (20 mM HEPES [pH 7.5], 150 mM NaCl, 0.01%, bovine serum albumin,
705 and 0.002% Tween-20) for 10 min before experiments began. The sequence of steps in
706 each assay was regeneration, custom, loading, baseline, association, and dissociation.
707 Every experiment was done at 25 °C with shaking at 1000 rpm. Technical replicates were
708 performed by using the same fiber tip and repeating the steps outlined previously.
709 Regeneration was performed by exposing the tips to regeneration buffer (Glycine pH 1.5)
710 for 5s and BLI buffer for 5s and repeating the exposure for 6 cycles. BLI buffer was used
711 for the custom, baseline, and dissociation steps; these steps were performed in the same
712 well for a given sample. For the dose response in **Figure 3A**, MBP-EFR3A was diluted in
713 BLI buffer to 200 nM and was loaded onto the anti penta-His biosensor tips. TTC7B-
714 FAM126A was also diluted in BLI buffer from 900 nM to 9.2 nM and added to the
715 appropriate association wells. Non-specific association was controlled by loading 200 nM
716 of His-MBP onto the biosensor tips and subtracting its responses from the responses
717 measured with MBP-EFR3A. The K_D was estimated by one site specific non-linear

718 regression analysis on GraphPad Prism 7.0 for Mac OS X, Graphpad Software,
719 www.graphpad.com.
720 For the mutant binding experiments, EFR3A was diluted in BLI buffer to 200 nM
721 and TTC7B-FAM126A was diluted in BLI buffer to 500 nM. All BLI experiments were
722 performed using two or three technical replicates. Means ± SD were used to present
723 values. Statistical analysis between conditions was performed using an unpaired t-test
724 assuming unequal variances analysing mutant responses to wildtype responses
725 measured simultaneously during each assay. The concentration of a given mutant was
726 compared with the same concentration for wild-type binding. The following legends are
727 used for statistical significance: ***$p<0.0001$, **$p<0.001$, *$p< 0.01$ and ns $p>0.01$.
728
729 ***Multiple Sequence Alignments***
730 Sequences were aligned using Clustal Omega Multiple Sequence Alignment, and the
731 aligned sequences were subsequently analysed by ESPript 3.0 (https://espript.ibcp.fr) to
732 visualize conserved regions (*49*). The UniProt accession codes for the aligned sequences
733 used for TTC7 in **Figure 3C** are Q86TV6 *(Homo sapiens)*, Q9ULT0 *(Homo sapiens)*,
734 E9Q6P5 *(Mus musculus)*, A0A8J1LRC8 *(Xenopus laevis)*, A0A8M2B4X5 *(Danio rerio),*
735 A0A0B4K7H0 *(Drosophila melanogaster)*. The UniProt accession codes for the aligned
736 sequences used for FAM126 in **Figure 4B** are Q9BYI3 *(Homo Sapiens)*, Q8IXS8 *(Homo*
737 *Sapiens)*, Q6P9N1 *(Mus musculus)*, Q6P121 *(Danio rerio)*, Q7K1C5 *(Drosophila*
738 *melanogaster)*, Q6A586 *(Caenorhabditis elegans)*. The UniProt accession codes for the
739 aligned sequences used for EFR3 in **Figures 3B, 4A and Supplemental Figure 1** are
740 Q14156 *(Homo Sapiens)*, Q9Y2G0 *(Homo sapiens)*, Q8BG67 *(Mus musculus)*, Q641A2
741 *(Xenopus laevis)*, Q5SPP5 *(Danio rerio)*, Q8IGJ0 *(Drosophila melanogaster)*, Q09263
742 *(Caenorhabditis elegans)*, O59817 *(Schizosaccharomyces pombe)*, Q03653
743 *(Saccharomyces cerevisiae)*.
744
745 ***Mammalian Cell Culture***
746 HEK293A (Invitrogen) cells were cultured in Dulbecco's Modified Eagle Medium (DMEM-
747 high glucose; Gibco) containing 10% (vol/vol) FBS and supplemented with a 1% solution

748 of penicillin/streptomycin (Gibco). Cells were maintained at 37°C and 5% CO_2 in a
749 humidified atmosphere and regularly tested for *Mycoplasma* contamination using a
750 commercially available detection kit (InvivoGen). After thawing, cell cultures are also
751 treated with plasmocin (InvivoGen) at 500 μg/mL for the initial three passages (6-9 days)
752 as well as supplemented with 5 μg/mL of the prophylactic for all subsequent passages.
753

754 ***Live-Cell Measurements using the PM-PI4KA^{BRET} Biosensor***

755 HEK293A cells (0.75x10^5 cells/well) were seeded in a 200 µL total volume to white-bottom
756 96 well plates pre-coated with 0.01% poly-L-lysine solution (Sigma) and cultured
757 overnight. Cells were then transfected with 0.5 µg of the PM-PI4KA^{BRET} biosensor (L10-
758 mVenus-tPT2A-nLuc-PI4KA) using Lipofectamine 2000 (1 µL/well). Lipofection was done
759 within Opti-MEM (40 µL/well) according to the manufacturer's protocol, but with the slight
760 modification of removing the media containing the Lipofectamine-complexed DNA and
761 replacing it with complete culture medium at between 4-6 hrs post-transfection. Where
762 indicated, increasing amounts (100, 500, or 1000 ng/well) of specified plasmids consisting
763 of either an empty vector (pcDNA3.1), wild-type positive control (EFR3B-P2A-TTC7B-
764 T2A-FAM126A), or the indicated mutants of the PI4KA complex components (EFR3B$^{\Delta}$
765 ^{cterm}-P2A-TTC7B-T2A-FAM126A, EFR3B^{L726A,F751A}-P2A-TTC7B-T2A-FAM126A, EFR3B-
766 P2A-TTC7B^{A702R}-T2A-FAM126A, or EFR3B-P2A-TTC7B-T2A-FAM126A^{A103R}) were co-
767 transfected (0.5-1.5 µg/well total). BRET measurements were made at 37°C using a
768 Tristar2 LB 942 Multimode Microplate Reader (Berthold Technologies) with customized
769 emission filters (540/40 nm and 475/20 nm). Between 20-24 hrs post-transfection, the
770 cells were quickly washed before being incubated for 30 mins in 50 μL of modified Krebs-
771 Ringer buffer (containing 120 mM NaCl, 4.7 mM KCl, 2 mM $CaCl_2$, 0.7 mM $MgSO_4$,
772 10 mM glucose, 10 mM HEPES, and adjusted to pH 7.4) at 37°C in a CO_2-independent
773 incubator. After the pre-incubation period, the cell-permeable luciferase substrate,
774 coelenterazine h (40 μL, final concentration 5 μM), was added and the signal from the
775 mVenus fluorescence and nLuc luminescence were recorded using 485 and 530 nm
776 emission filters over a 45 min baseline BRET measurement (90 sec / cycle). Detection

time was always 500 ms for each wavelength. To ensure a stable baseline is achieved following the substrate addition, BRET measurements are presented as the average basal BRET signal over the final 30 minutes measurement interval (15-45 minutes). All measurements were carried out in triplicate wells and repeated in three independent experiments. From each well, the BRET ratio was calculated by dividing the 530 nm and 485 nm intensities, which were then normalized to an internal measurement of wells transfected with the PM-PI4KA^{BRET} biosensor alone.

Live-cell Confocal Microscopy of EGFP-PI4KA Localization

HEK293A cells (2.5×10^5 cells/dish) were plated with a final volume of 1.5 mL on 29 mm circular glass-bottom culture dishes (#1.5; Cellvis) pre-coated with 0.01% poly-L-lysine solution (Sigma). Cells were allowed to attach overnight prior to transfection with plasmid DNAs (0.5-0.75 µg/well) using Lipofectamine 2000 (2-5 µL/well; Invitrogen). Lipofection was done using small volumes of Opti-MEM (200 µL; Invitrogen) according to the manufacturer's instructions, once again with the slight modification of removing the media containing the Lipofectamine-complexed DNA at 4-6 hrs post-transfection and replacing it with complete DMEM. After 18-20 hrs of transfection, cells were incubated in 1 mL of modified Krebs-Ringer solution (containing 120 mM NaCl, 4.7 mM KCl, 2 mM $CaCl_2$, 0.7 mM $MgSO_4$, 10 mM glucose, 10 mM HEPES, and adjusted to pH 7.4) and images were acquired at room temperature using a Zeiss LSM 880 (63x/1.40 N.A. Plan-Apochromat Oil DIC M27 Objective) laser-scanning confocal microscopes (Carl Zeiss Microscopy). Image acquisition was performed using the ZEN software system (Carl Zeiss Microscopy), while image preparation and analysis was done using the open-source FIJI platform(*50*).

References

1. T. Balla, Phosphoinositides: tiny lipids with giant impact on cell regulation. *Physiol. Rev.* **93**, 1019–1137 (2013).
2. J. E. Burke, J. Triscott, B. M. Emerling, G. R. V. Hammond, Beyond PI3Ks: targeting phosphoinositide kinases in disease. *Nat Rev Drug Discov*, 1–30 (2022).
3. G. R. V. Hammond, J. E. Burke, Novel roles of phosphoinositides in signaling, lipid transport, and disease. *Curr Opin Cell Biol* **63**, 57–67 (2020).

4. A. G. Batrouni, J. M. Baskin, The chemistry and biology of phosphatidylinositol 4-phosphate at the plasma membrane. *Bioorg Med Chem* **40**, 116190 (2021).
5. F. Nakatsu, J. M. Baskin, J. Chung, L. B. Tanner, G. Shui, S. Y. Lee, M. Pirruccello, M. Hao, N. T. Ingolia, M. R. Wenk, P. De Camilli, PtdIns4P synthesis by PI4KIIIα at the plasma membrane and its impact on plasma membrane identity. *J. Cell Biol.* **199**, 1003–1016 (2012).
6. J. Chung, F. Torta, K. Masai, L. Lucast, H. Czapla, L. B. Tanner, P. Narayanaswamy, M. R. Wenk, F. Nakatsu, P. De Camilli, INTRACELLULAR TRANSPORT. PI4P/phosphatidylserine countertransport at ORP5- and ORP8-mediated ER-plasma membrane contacts. *Science* **349**, 428–432 (2015).
7. R. G. de Rubio, R. F. Ransom, S. Malik, D. I. Yule, A. Anantharam, A. V. Smrcka, Phosphatidylinositol 4-phosphate is a major source of GPCR-stimulated phosphoinositide production. *Sci Signal* **11**, eaan1210 (2018).
8. I. Barlow-Busch, A. L. Shaw, J. E. Burke, PI4KA and PIKfyve: Essential phosphoinositide signaling enzymes involved in myriad human diseases. *Curr Opin Cell Biol* **83**, 102207 (2023).
9. C. G. Salter, Y. Cai, B. Lo, G. Helman, H. Taylor, A. McCartney, J. S. Leslie, A. Accogli, F. Zara, M. Traverso, J. Fasham, J. A. Lees, M. P. Ferla, B. A. Chioza, O. Wenger, E. Scott, H. E. Cross, J. Crawford, I. Warshawsky, M. Keisling, D. Agamanolis, C. Ward Melver, H. Cox, M. Elawad, T. Marton, M. N. Wakeling, D. Holzinger, S. Tippelt, M. Munteanu, D. Valcheva, C. Deal, S. Van Meerbeke, C. Walsh Vockley, M. J. Butte, U. Acar, M. S. van der Knaap, G. C. Korenke, U. Kotzaeridou, T. Balla, C. Simons, H. H. Uhlig, A. H. Crosby, P. De Camilli, N. I. Wolf, E. L. Baple, Biallelic PI4KA variants cause neurological, intestinal and immunological disease. *Brain* **144**, 3597–3610 (2021).
10. E. Verdura, A. Rodríguez-Palmero, V. Vélez-Santamaria, L. Planas-Serra, I. de la Calle, M. Raspall-Chaure, A. Roubertie, M. Benkirane, F. Saettini, L. Pavinato, G. Mandrile, M. O'Leary, E. O'Heir, E. Barredo, A. Chacón, V. Michaud, C. Goizet, M. Ruiz, A. Schlüter, I. Rouvet, J. Sala-Coromina, C. Fossati, M. Iascone, F. Canonico, A. Marcé-Grau, P. de Souza, D. R. Adams, C. Casasnovas, H. L. Rehm, H. C. Mefford, L. González Gutierrez-Solana, A. Brusco, M. Koenig, A. Macaya, A. Pujol, Biallelic PI4KA variants cause a novel neurodevelopmental syndrome with hypomyelinating leukodystrophy. *Brain* **144**, 2659–2669 (2021).
11. R. Chen, S. Giliani, G. Lanzi, G. I. Mias, S. Lonardi, K. Dobbs, J. Manis, H. Im, J. E. Gallagher, D. H. Phanstiel, G. Euskirchen, P. Lacroute, K. Bettinger, D. Moratto, K. Weinacht, D. Montin, E. Gallo, G. Mangili, F. Porta, L. D. Notarangelo, S. Pedretti, W. Al-Herz, W. Alfahdli, A. M. Comeau, R. S. Traister, S.-Y. Pai, G. Carella, F. Facchetti, K. C. Nadeau, M. Snyder, L. D. Notarangelo, Whole-exome sequencing identifies tetratricopeptide repeat domain 7A (TTC7A) mutations for combined immunodeficiency with intestinal atresias. *J. Allergy Clin. Immunol.* **132**, 656-664.e17 (2013).
12. A. E. Bigorgne, H. F. Farin, R. Lemoine, N. Mahlaoui, N. Lambert, M. Gil, A. Schulz, P. Philippet, P. Schlesser, T. G. Abrahamsen, K. Oymar, E. G. Davies, C. L. Ellingsen, E. Leteurtre, B. Moreau-Massart, D. Berrebi, C. Bole-Feysot, P.

853 Nischke, N. Brousse, A. Fischer, H. Clevers, G. de Saint Basile, TTC7A mutations
854 disrupt intestinal epithelial apicobasal polarity. *J Clin Invest* **124**, 328–337 (2014).
855 13. Y. Avitzur, C. Guo, L. A. Mastropaolo, E. Bahrami, H. Chen, Z. Zhao, A. Elkadri, S.
856 Dhillon, R. Murchie, R. Fattouh, H. Huynh, J. L. Walker, P. W. Wales, E. Cutz, Y.
857 Kakuta, J. Dudley, J. Kammermeier, F. Powrie, N. Shah, C. Walz, M. Nathrath, D.
858 Kotlarz, J. Puchaka, J. R. Krieger, T. Racek, T. Kirchner, T. D. Walters, J. H.
859 Brumell, A. M. Griffiths, N. Rezaei, P. Rashtian, M. Najafi, M. Monajemzadeh, S.
860 Pelsue, D. P. B. McGovern, H. H. Uhlig, E. Schadt, C. Klein, S. B. Snapper, A. M.
861 Muise, Mutations in tetratricopeptide repeat domain 7A result in a severe form of
862 very early onset inflammatory bowel disease. *Gastroenterology* **146**, 1028–1039
863 (2014).
864 14. H. Adhikari, W. E. Kattan, S. Kumar, P. Zhou, J. F. Hancock, C. M. Counter,
865 Oncogenic KRAS is dependent upon an EFR3A-PI4KA signaling axis for potent
866 tumorigenic activity. *Nat Commun* **12**, 5248 (2021).
867 15. W. E. Kattan, J. Liu, D. Montufar-Solis, H. Liang, B. Brahmendra Barathi, R. van
868 der Hoeven, Y. Zhou, J. F. Hancock, Components of the phosphatidylserine
869 endoplasmic reticulum to plasma membrane transport mechanism as targets for
870 KRAS inhibition in pancreatic cancer. *Proc Natl Acad Sci USA* **118**, e2114126118
871 (2021).
872 16. K. L. Berger, J. D. Cooper, N. S. Heaton, R. Yoon, T. E. Oakland, T. X. Jordan, G.
873 Mateu, A. Grakoui, G. Randall, Roles for endocytic trafficking and
874 phosphatidylinositol 4-kinase III alpha in hepatitis C virus replication. *Proc. Natl.*
875 *Acad. Sci. U.S.A.* **106**, 7577–7582 (2009).
876 17. J. E. Burke, Structural Basis for Regulation of Phosphoinositide Kinases and Their
877 Involvement in Human Disease. *Mol. Cell* **71**, 653–673 (2018).
878 18. J. A. Lees, Y. Zhang, M. S. Oh, C. M. Schauder, X. Yu, J. M. Baskin, K. Dobbs, L.
879 D. Notarangelo, P. De Camilli, T. Walz, K. M. Reinisch, Architecture of the human
880 PI4KIIIα lipid kinase complex. *Proc. Natl. Acad. Sci. U.S.A.* **114**, 13720–13725
881 (2017).
882 19. J. M. Baskin, X. Wu, R. Christiano, M. S. Oh, C. M. Schauder, E. Gazzerro, M.
883 Messa, S. Baldassari, S. Assereto, R. Biancheri, F. Zara, C. Minetti, A. Raimondi,
884 M. Simons, T. C. Walther, K. M. Reinisch, P. De Camilli, The leukodystrophy
885 protein FAM126A (hyccin) regulates PtdIns(4)P synthesis at the
886 plasma membrane. *Nat. Cell Biol.* **18**, 132–138 (2016).
887 20. S. Suresh, J. E. Burke, Structural basis for the conserved roles of PI4KA and its
888 regulatory partners and their misregulation in disease. *Adv Biol Regul* **90**, 100996
889 (2023).
890 21. G. L. Dornan, U. Dalwadi, D. J. Hamelin, R. M. Hoffmann, C. K. Yip, J. E. Burke,
891 Probing the Architecture, Dynamics, and Inhibition of the PI4KIIIα/TTC7/FAM126
892 Complex. *J. Mol. Biol.* **430**, 3129–3142 (2018).
893 22. N. Bojjireddy, M. L. Guzman-Hernandez, N. R. Reinhard, M. Jovic, T. Balla, EFR3s
894 are palmitoylated plasma membrane proteins that control responsiveness to G
895 protein-coupled receptors. *J. Cell. Sci.*, doi: 10.1242/jcs.157495 (2014).

23. A. G. Batrouni, N. Bag, H. T. Phan, B. A. Baird, J. M. Baskin, A palmitoylation code controls PI4KIIIα complex formation and PI(4,5)P2 homeostasis at the plasma membrane. *J Cell Sci* **135**, jcs259365 (2022).
24. D. Baird, C. Stefan, A. Audhya, S. Weys, S. D. Emr, Assembly of the PtdIns 4-kinase Stt4 complex at the plasma membrane requires Ypp1 and Efr3. *J. Cell Biol.* **183**, 1061–1074 (2008).
25. X. Wu, R. J. Chi, J. M. Baskin, L. Lucast, C. G. Burd, P. De Camilli, K. M. Reinisch, Structural insights into assembly and regulation of the plasma membrane phosphatidylinositol 4-kinase complex. *Developmental Cell* **28**, 19–29 (2014).
26. J. Myeong, L. de la Cruz, S.-R. Jung, J.-H. Yeon, B.-C. Suh, D.-S. Koh, B. Hille, Phosphatidylinositol 4,5-bisphosphate is regenerated by speeding of the PI 4-kinase pathway during long PLC activation. *J Gen Physiol* **152**, e202012627 (2020).
27. J. Jumper, R. Evans, A. Pritzel, T. Green, M. Figurnov, O. Ronneberger, K. Tunyasuvunakool, R. Bates, A. Žídek, A. Potapenko, A. Bridgland, C. Meyer, S. A. A. Kohl, A. J. Ballard, A. Cowie, B. Romera-Paredes, S. Nikolov, R. Jain, J. Adler, T. Back, S. Petersen, D. Reiman, E. Clancy, M. Zielinski, M. Steinegger, M. Pacholska, T. Berghammer, S. Bodenstein, D. Silver, O. Vinyals, A. W. Senior, K. Kavukcuoglu, P. Kohli, D. Hassabis, Highly accurate protein structure prediction with AlphaFold. *Nature* **596**, 583–589 (2021).
28. M. Mirdita, K. Schütze, Y. Moriwaki, L. Heo, S. Ovchinnikov, M. Steinegger, ColabFold: making protein folding accessible to all. *Nat Methods* **19**, 679–682 (2022).
29. E. I. James, T. A. Murphree, C. Vorauer, J. R. Engen, M. Guttman, Advances in Hydrogen/Deuterium Exchange Mass Spectrometry and the Pursuit of Challenging Biological Systems. *Chem Rev* **122**, 7562–7623 (2022).
30. G. R. Masson, M. L. Jenkins, J. E. Burke, An overview of hydrogen deuterium exchange mass spectrometry (HDX-MS) in drug discovery. *Expert Opin Drug Discov* **12**, 981–994 (2017).
31. G. R. Masson, J. E. Burke, N. G. Ahn, G. S. Anand, C. Borchers, S. Brier, G. M. Bou-Assaf, J. R. Engen, S. W. Englander, J. Faber, R. Garlish, P. R. Griffin, M. L. Gross, M. Guttman, Y. Hamuro, A. J. R. Heck, D. Houde, R. E. Iacob, T. J. D. Jørgensen, I. A. Kaltashov, J. P. Klinman, L. Konermann, P. Man, L. Mayne, B. D. Pascal, D. Reichmann, M. Skehel, J. Snijder, T. S. Strutzenberg, E. S. Underbakke, C. Wagner, T. E. Wales, B. T. Walters, D. D. Weis, D. J. Wilson, P. L. Wintrode, Z. Zhang, J. Zheng, D. C. Schriemer, K. D. Rand, Recommendations for performing, interpreting and reporting hydrogen deuterium exchange mass spectrometry (HDX-MS) experiments. *Nat. Methods* **16**, 595–602 (2019).
32. I. Ulengin-Talkish, M. A. H. Parson, M. L. Jenkins, J. Roy, A. Z. L. Shih, N. St-Denis, G. Gulyas, T. Balla, A.-C. Gingras, P. Várnai, E. Conibear, J. E. Burke, M. S. Cyert, Palmitoylation targets the calcineurin phosphatase to the phosphatidylinositol 4-kinase complex at the plasma membrane. *Nat Commun* **12**, 6064 (2021).

939 33. N. S. Agarwal, L. Northrop, K. Anyane-Yeboa, V. S. Aggarwal, P. L. Nagy, Y. Y.
940 Demirdag, Tetratricopeptide repeat domain 7A (TTC7A) mutation in a newborn with
941 multiple intestinal atresia and combined immunodeficiency. *J. Clin. Immunol.* **34**,
942 607–610 (2014).
943 34. S. Jardine, N. Dhingani, A. M. Muise, TTC7A: Steward of Intestinal Health. *Cell Mol*
944 *Gastroenterol Hepatol* **7**, 555–570 (2019).
945 35. M. Varadi, S. Anyango, M. Deshpande, S. Nair, C. Natassia, G. Yordanova, D.
946 Yuan, O. Stroe, G. Wood, A. Laydon, A. Žídek, T. Green, K. Tunyasuvunakool, S.
947 Petersen, J. Jumper, E. Clancy, R. Green, A. Vora, M. Lutfi, M. Figurnov, A. Cowie,
948 N. Hobbs, P. Kohli, G. Kleywegt, E. Birney, D. Hassabis, S. Velankar, AlphaFold
949 Protein Structure Database: massively expanding the structural coverage of
950 protein-sequence space with high-accuracy models. *Nucleic Acids Research* **50**,
951 D439–D444 (2022).
952 36. P. V. Hornbeck, B. Zhang, B. Murray, J. M. Kornhauser, V. Latham, E. Skrzypek,
953 PhosphoSitePlus, 2014: mutations, PTMs and recalibrations. *Nucleic Acids Res.*
954 **43**, D512-20 (2015).
955 37. J. Chung, F. Nakatsu, J. M. Baskin, P. De Camilli, Plasticity of PI4KIIIα interactions
956 at the plasma membrane. *EMBO Rep.* **16**, 312–320 (2015).
957 38. Y. Perez-Riverol, J. Bai, C. Bandla, D. García-Seisdedos, S. Hewapathirana, S.
958 Kamatchinathan, D. J. Kundu, A. Prakash, A. Frericks-Zipper, M. Eisenacher, M.
959 Walzer, S. Wang, A. Brazma, J. A. Vizcaíno, The PRIDE database resources in
960 2022: a hub for mass spectrometry-based proteomics evidences. *Nucleic Acids*
961 *Res* **50**, D543–D552 (2022).
962 39. D. G. Gibson, L. Young, R.-Y. Chuang, J. C. Venter, C. A. Hutchison, H. O. Smith,
963 Enzymatic assembly of DNA molecules up to several hundred kilobases. *Nat.*
964 *Methods* **6**, 343–345 (2009).
965 40. J. T. Tóth, G. Gulyás, D. J. Tóth, A. Balla, G. R. V. Hammond, L. Hunyady, T.
966 Balla, P. Várnai, BRET-monitoring of the dynamic changes of inositol lipid pools in
967 living cells reveals a PKC-dependent PtdIns4P increase upon EGF and M3
968 receptor activation. *Biochim Biophys Acta* **1861**, 177–187 (2016).
969 41. Z. Liu, O. Chen, J. B. J. Wall, M. Zheng, Y. Zhou, L. Wang, H. R. Vaseghi, L. Qian,
970 J. Liu, Systematic comparison of 2A peptides for cloning multi-genes in a
971 polycistronic vector. *Sci Rep* **7**, 2193 (2017).
972 42. G. R. V. Hammond, M. P. Machner, T. Balla, A novel probe for phosphatidylinositol
973 4-phosphate reveals multiple pools beyond the Golgi. *J Cell Biol* **205**, 113–126
974 (2014).
975 43. J. Abramson, J. Adler, J. Dunger, R. Evans, T. Green, A. Pritzel, O. Ronneberger,
976 L. Willmore, A. J. Ballard, J. Bambrick, S. W. Bodenstein, D. A. Evans, C.-C. Hung,
977 M. O'Neill, D. Reiman, K. Tunyasuvunakool, Z. Wu, A. Žemgulytė, E. Arvaniti, C.
978 Beattie, O. Bertolli, A. Bridgland, A. Cherepanov, M. Congreve, A. I. Cowen-Rivers,
979 A. Cowie, M. Figurnov, F. B. Fuchs, H. Gladman, R. Jain, Y. A. Khan, C. M. R.
980 Low, K. Perlin, A. Potapenko, P. Savy, S. Singh, A. Stecula, A. Thillaisundaram, C.
981 Tong, S. Yakneen, E. D. Zhong, M. Zielinski, A. Žídek, V. Bapst, P. Kohli, M.

Jaderberg, D. Hassabis, J. M. Jumper, Accurate structure prediction of biomolecular interactions with AlphaFold 3. *Nature* **630**, 493–500 (2024).

44. E. F. Pettersen, T. D. Goddard, C. C. Huang, G. S. Couch, D. M. Greenblatt, E. C. Meng, T. E. Ferrin, UCSF Chimera--a visualization system for exploratory research and analysis. *J Comput Chem* **25**, 1605–1612 (2004).
45. P. V. Afonine, R. W. Grosse-Kunstleve, N. Echols, J. J. Headd, N. W. Moriarty, M. Mustyakimov, T. C. Terwilliger, A. Urzhumtsev, P. H. Zwart, P. D. Adams, Towards automated crystallographic structure refinement with phenix.refine. *Acta Crystallogr. D Biol. Crystallogr.* **68**, 352–367 (2012).
46. J. T. B. Stariha, R. M. Hoffmann, D. J. Hamelin, J. E. Burke, Probing Protein-Membrane Interactions and Dynamics Using Hydrogen-Deuterium Exchange Mass Spectrometry (HDX-MS). *Methods Mol Biol* **2263**, 465–485 (2021).
47. J. M. Dobbs, M. L. Jenkins, J. E. Burke, Escherichia coli and Sf9 Contaminant Databases to Increase Efficiency of Tandem Mass Spectrometry Peptide Identification in Structural Mass Spectrometry Experiments. *J Am Soc Mass Spectrom* **31**, 2202–2209 (2020).
48. A. T. Kong, F. V. Leprevost, D. M. Avtonomov, D. Mellacheruvu, A. I. Nesvizhskii, MSFragger: ultrafast and comprehensive peptide identification in mass spectrometry-based proteomics. *Nat Methods* **14**, 513–520 (2017).
49. P. Gouet, X. Robert, E. Courcelle, ESPript/ENDscript: Extracting and rendering sequence and 3D information from atomic structures of proteins. *Nucleic Acids Res.* **31**, 3320–3323 (2003).
50. J. Schindelin, I. Arganda-Carreras, E. Frise, V. Kaynig, M. Longair, T. Pietzsch, S. Preibisch, C. Rueden, S. Saalfeld, B. Schmid, J.-Y. Tinevez, D. J. White, V. Hartenstein, K. Eliceiri, P. Tomancak, A. Cardona, Fiji: an open-source platform for biological-image analysis. *Nat. Methods* **9**, 676–682 (2012).

1020 **Figures**

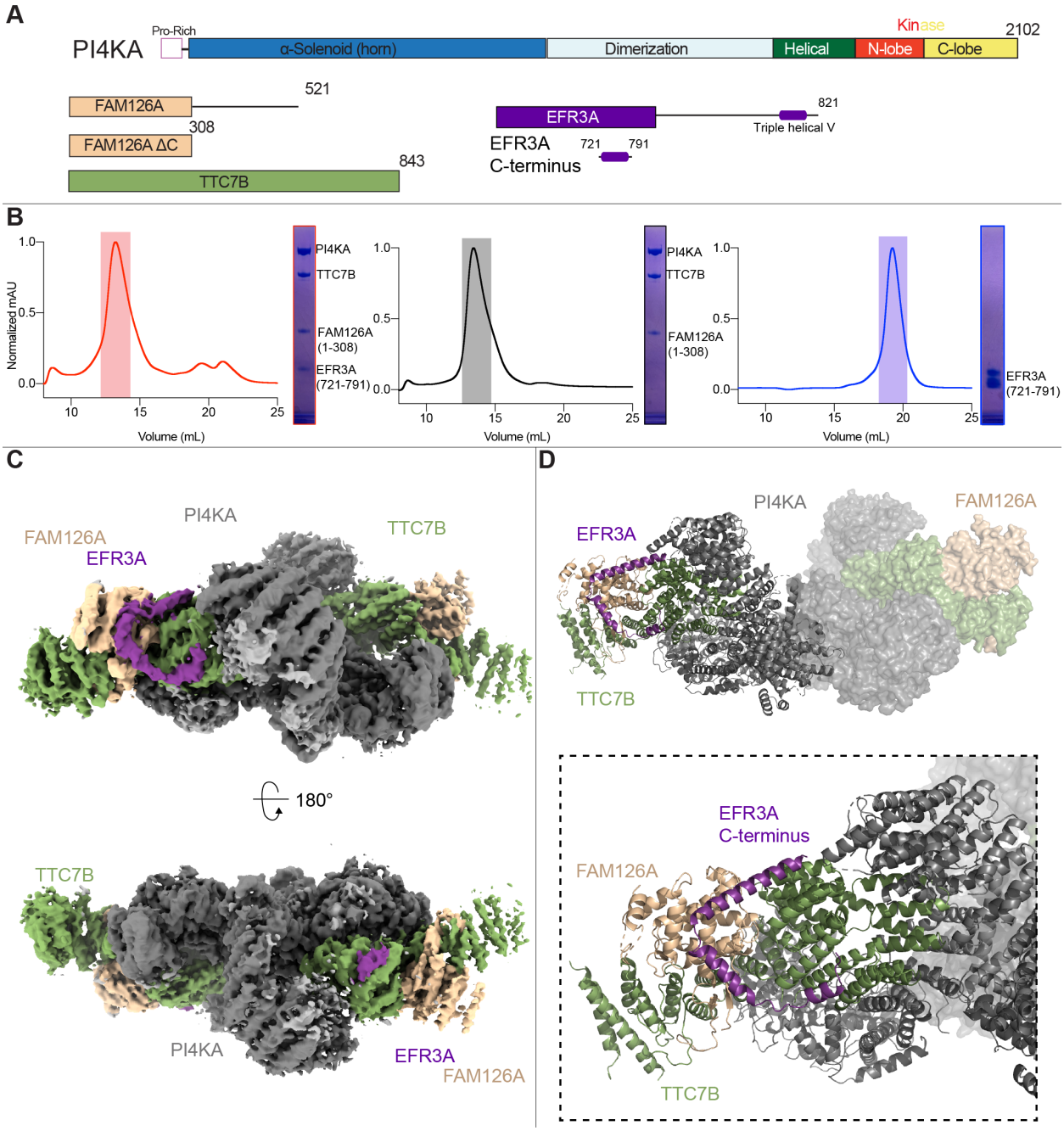

1021

1022 **Figure 1. Cryo-EM analysis of EFR3 binding to the PI4KA complex**

1023 **A.** Domain schematics of the full-length PI4KA complex and EFR3A constructs used in this paper.
1024 Constructs used in this paper are PI4KA/TTC7B/FAM126A ΔC (referred to as PI4KA complex) and
1025 EFR3A (721-791) referred to as EFR3A.

1026 **B.** Size exclusion chromatography traces of (L) PI4KA complex/EFR3A, (M) PI4KA complex, and (R)
1027 EFR3A, with corresponding SDS-PAGE gels to show protein present in the highlighted size exclusion
1028 chromatography (SEC) peaks.

1029 **C.** Cryo-EM density map of the PI4KA complex bound to EFR3A. EFR3A was bound to both sides of the
1030 hetero-trimer, however, the full triple helical V was only visible in one of the two dimers of hetero-
1031 tetramers (see left side of the molecule in the top panel).
1032 **D.** Molecular model of the triple helical V in the C-terminus of EFR3A (724-787) bound to the PI4KA
1033 complex, with a zoom-in highlighting EFR3A contacts with both TTC7B and FAM126A.
1034
1035
1036
1037
1038

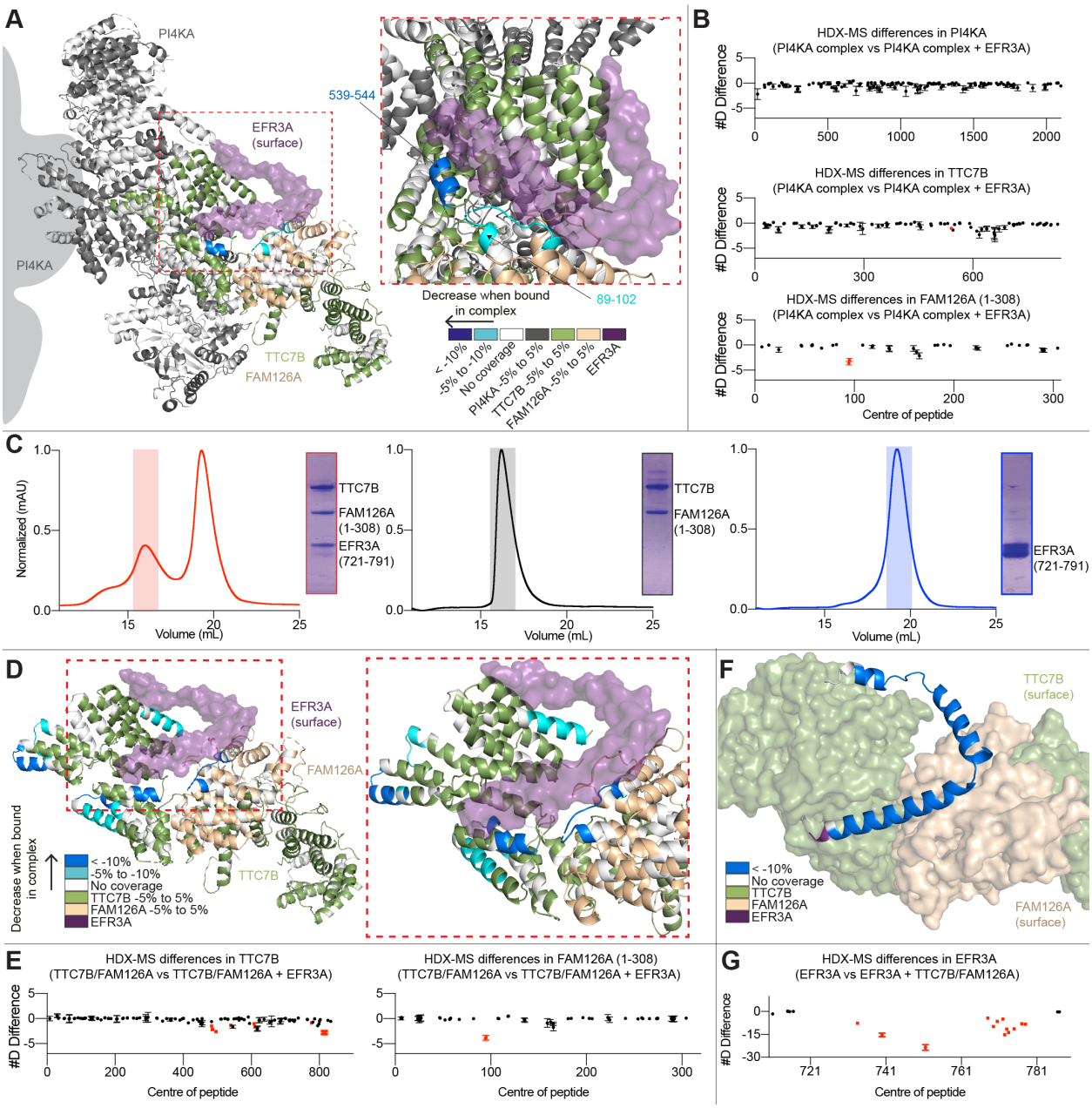

Figure 2: HDX-MS analysis of the interaction of EFR3A with TTC7B and FAM126A

A. Residues showing significant differences in deuterium exchange (defined as >5% 0.45 Da, and p<0.01 in an unpaired two-tailed t-test at any time point) upon PI4KA complex binding to EFR3A. Differences are mapped on a structural model of the high local resolution half, with a zoom-in on the interface. Differences are indicated by the legend.

B. Sum of the number of deuteron differences of PI4KA complex upon formation with EFR3A analysed over the entire deuterium exchange time course for the PI4KA complex. Each point is representative of the centre residue of an individual peptide. Peptides that met the significance criteria described in A are

1048 coloured red. Error is shown as the sum of standard deviations across all 4 time points (SD) (n=3 for each
1049 condition in each timepoint).
1050 **C.** Size exclusion chromatography traces of (L) TTC7B-FAM126A ΔC -EFR3A, (M) TTC7B-FAM126A
1051 ΔC, and (R) EFR3A, with corresponding SDS-PAGE gels to show protein present in the highlighted SEC
1052 peaks.
1053 **D.** TTC7B-FAM126A residues showing significant differences in deuterium exchange (defined as >5%
1054 0.45 Da, and $p<0.01$ in an unpaired two-tailed t-test at any time point) upon formation of the TTC7B-
1055 FAM126A-EFR3A complex. Differences are mapped on a structural model of the high local resolution half
1056 removing PI4KA, with a zoom in on the interface. Differences are indicated by the legend.
1057 **E.** Sum of the number of deuteron differences of TTC7B and FAM126A upon complex formation with
1058 EFR3A analysed over the entire deuterium exchange time course for the dimer. Each point is
1059 representative of the centre residue of an individual peptide. Peptides that met the significance criteria
1060 described in D are coloured red. Error is shown as the sum of standard deviations across all 5 time points
1061 (SD) (n=3 for each condition in each timepoint).
1062 **F.** EFR3A residues showing significant differences in deuterium exchange (defined as >5% 0.45 Da, and
1063 $p<0.01$ in an unpaired two-tailed t-test at any time point) upon formation of the TTC7B-FAM126A-EFR3A
1064 complex. Differences are mapped on a structural model of the high local resolution half removing PI4KA
1065 zooming in on the interface. Differences are indicated by the legend. The construct used has overlapping
1066 MBP peptides that do not contain EFR3A residues, therefore peptides that start before 721 are not
1067 EFR3A sequence.
1068 **G.** Sum of the number of deuteron differences of EFR3A upon complex formation with TTC7B-FAM126A
1069 analysed over the entire deuterium exchange time course for the EFR3A. Each point is representative of
1070 the centre residue of an individual peptide. Peptides that met the significance criteria described in F are
1071 coloured red. Error is shown as the sum of standard deviations across all 4 time points (SD) (n=3 for each
1072 condition in each timepoint). Individual deuterium exchange curves for significant differences for all
1073 conditions are shown in Supplemental Fig 4.

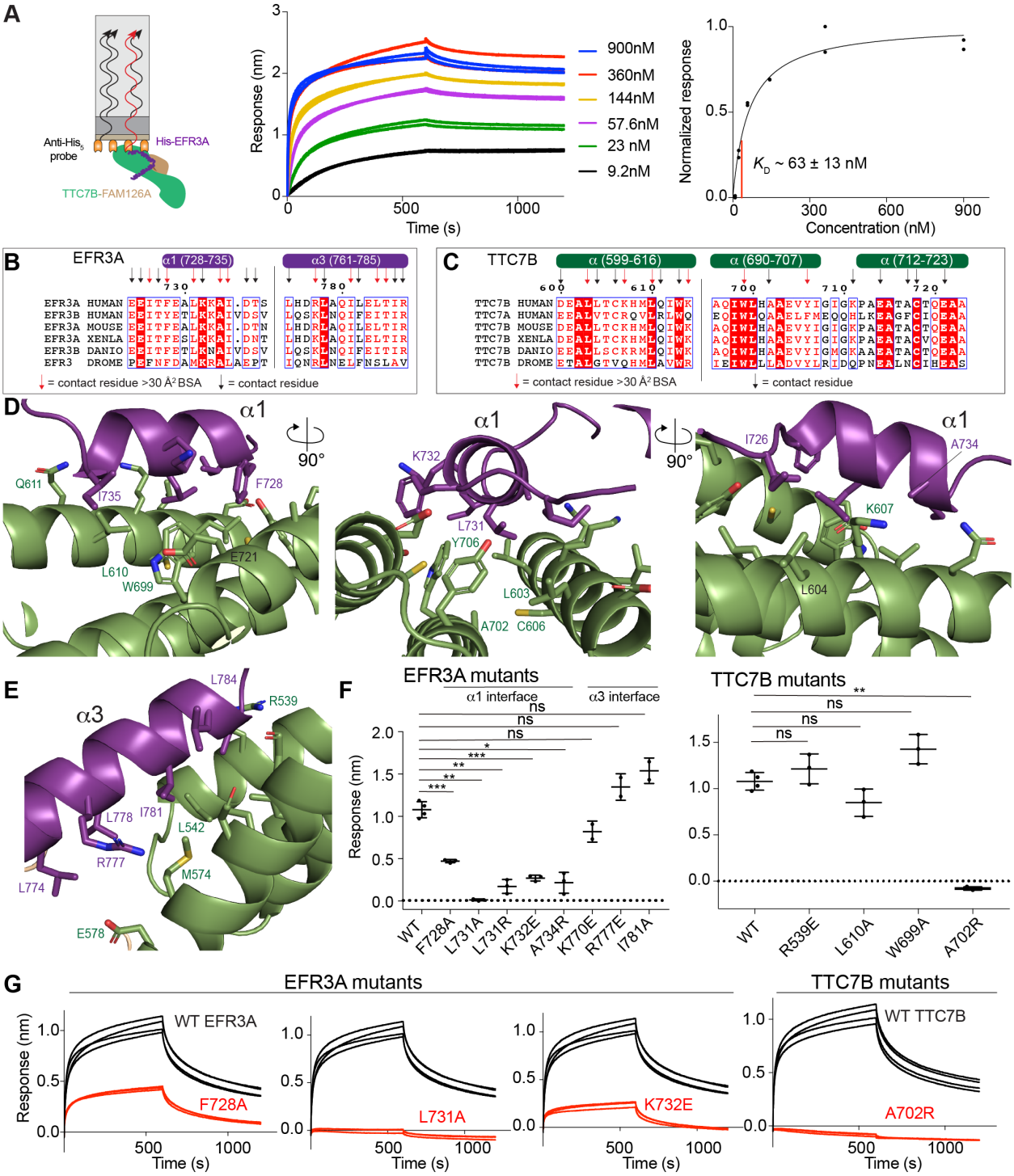

Figure 3: Molecular basis of EFR3A binding to TTC7B

A. Cartoon schematic (L) of a bio-layer interferometry (BLI) experiment showing binding of immobilized His-EFR3A (721-791) to TTC7B-FAM126A. Association and dissociation curves (M) for the binding of His-EFR3A (721-791) to different concentrations of TTC7B-FAM126A (10-2500 nM). The experiment was carried out in duplicate, with all data shown. Normalized BLI response versus concentration of TTC7B-

1080 FAM126A (R), with K_D estimated by one site specific non-linear regression. Each data point is shown
1081 (n=2).
1082 **B.** Multiple sequence alignment of EFR3A from *Homo sapiens, Mus musculus, Xenopus laevis, Danio*
1083 *rerio, Drosophila melanogaster*. EFR3A secondary structure of α1 and α3 helices are annotated above
1084 the alignment. Contact residues within 6 Å of TTC7B are annotated using arrows. Contact residues with
1085 BSA > 30 $Å^2$ are annotated using red arrows.
1086 **C.** Multiple sequence alignment of TTC7B from *Homo sapiens, Mus musculus, Xenopus laevis, Danio*
1087 *rerio, Drosophila melanogaster*. TTC7B secondary structure is annotated above the alignment. Contact
1088 residues within 6 Å of EFR3A are annotated using arrows. Contact residues with BSA > 30 $Å^2$ are
1089 annotated using red arrows.
1090 **D.** Zoomed in cartoon view of the EFR3A α1-TTC7B interface with putative interfacial residues labelled.
1091 EFR3A and TTC7B are coloured according to in-figure text.
1092 **E.** Zoomed in cartoon view of the EFR3A α3-TTC7B interface with putative interfacial residues labelled.
1093 EFR3A and TTC7B are coloured according to in-figure text.
1094 **F.** Maximum BLI response of various EFR3A and TTC7B mutants compared to WT. Error is shown as
1095 standard deviation (n=3) with two-tailed p values indicated as follows: **p<0.001; ***p<0.0001; not
1096 significant (ns) > 0.01.
1097 **G.** Raw BLI association and dissociation curves of EFR3A and TTC7B mutants compared to WT. His-
1098 EFR3A was loaded on the anti-penta-His tip at 200 nM and dipped in TTC7B-FAM126A at 500 nM. Raw
1099 BLI curves of all mutants in Supplemental Fig 5.

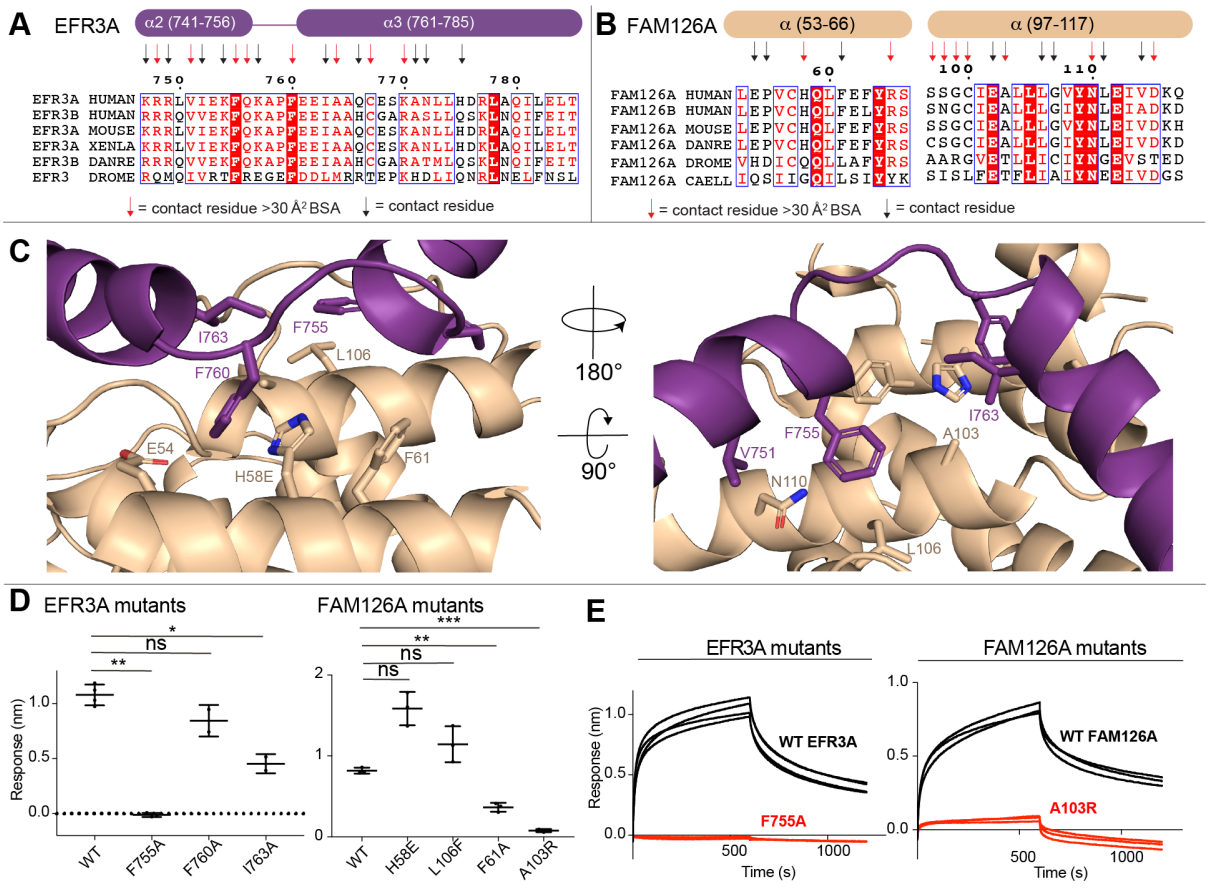

Figure 4. Mutational analysis validates the EFR3A-FAM126A binding interface

A. Multiple sequence alignment of EFR3A from *Homo sapiens, Mus musculus, Xenopus laevis, Danio rerio and Drosophila melanogaster*. EFR3A secondary structure of α2 and α3 helices are annotated above the alignment. Contact residues within 5 Å of FAM126A are annotated using arrows. Contact residues with BSA > 30 Å² are annotated using red arrows.

B. Multiple sequence alignment of FAM126A from *Homo sapiens, Mus musculus, Danio rerio, Drosophila melanogaster and Caenorhabditis elegans*. FAM126A secondary structure is annotated above the alignment. Contact residues within 5 Å of EFR3A are annotated using arrows. Contact residues with BSA > 30 Å² are annotated using red arrows.

C. Zoomed in cartoon view of the EFR3A-FAM126A interface with putative interfacial residues labelled. EFR3A and FAM126A are coloured according to in-figure text.

D. Maximum BLI response of various EFR3A and FAM126A mutants compared to WT. Error is shown as standard deviation (n=3) with p values indicated as follows: *p<0.01; **p<0.001; ***p<0.0001; not significant (ns) > 0.01.

E. Raw BLI association and dissociation curves of EFR3A and FAM126A mutants compared to WT. His-EFR3A was loaded on the anti-penta-His tip at 200 nM and dipped in TTC7B-FAM126A at 500 nM. Raw BLI curves of all mutants in Supplemental Fig 5.

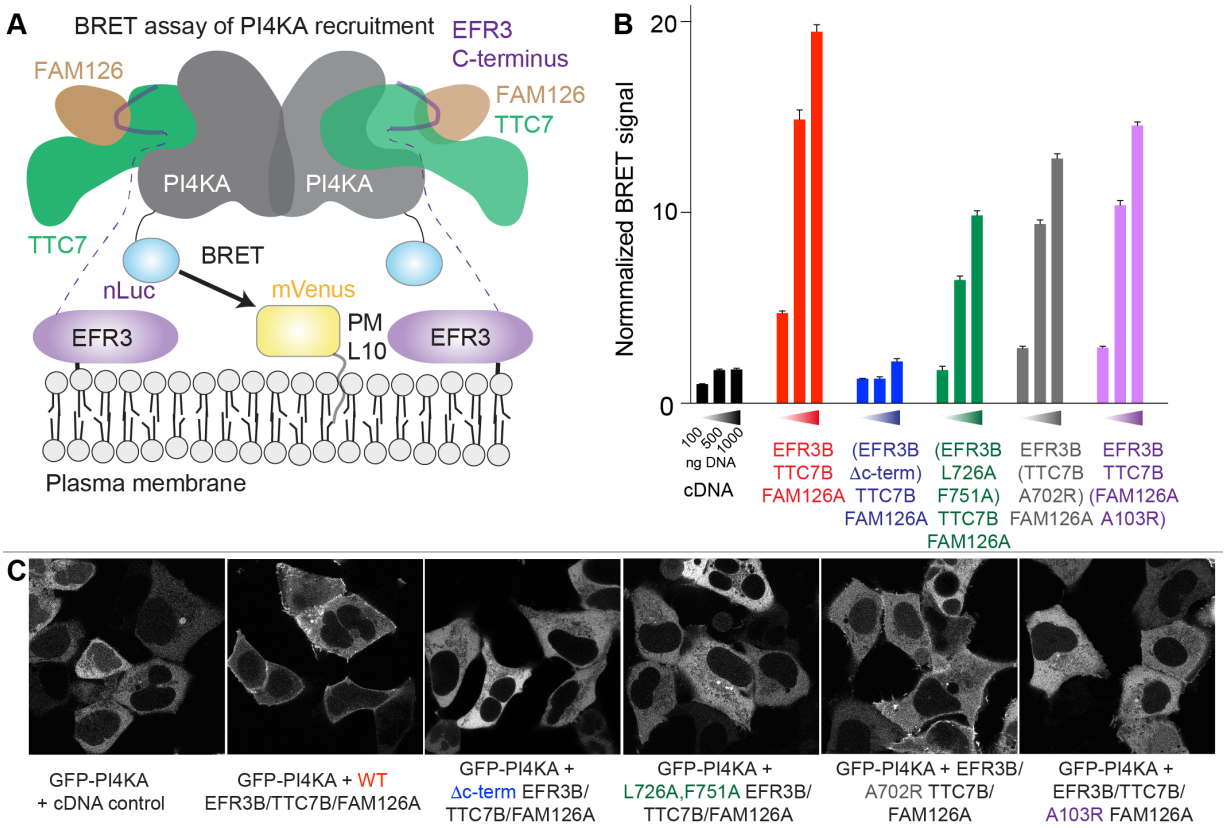

Figure 5. The C-terminus of EFR3A mediates plasma membrane recruitment of PI4KA

A. Cartoon depicting the quantitative BRET-based PI4KA recruitment assay. Briefly, the PM-anchored BRET acceptor (L10-mVenus) will only be near the nLuc-tagged PI4KA BRET-donor, and thereby efficiently increase the relative BRET signal, if co-assembled with the requisite molecular partners for PM targeting.

B. Normalized BRET signal measured from HEK293A cell populations (~0.75 x 10^5 cells/well) expressing a fixed amount of the PM-PI4KA^{BRET} biosensor (L10-mVenus-tPT2A-NLuc-PI4KA; 500 ng/ well) together with increasing amounts (100, 500, or 1000 ng/well) of constructs consisting of either an empty vector (black), wild-type control (red; EFR3B-P2A-TTC7B-T2A-FAM126A), or the indicated mutants of the PI4KA complex components (blue, EFR3B Δc-term(1-716)-P2A-TTC7B-T2A-FAM126A; green, EFR3B^{L726A,F751A}-P2A-TTC7B-T2A-FAM126A; grey, EFR3B-P2A-TTC7B^{A702R}-T2A-FAM126A; and, magenta, EFR3B-P2A-TTC7B-T2A-FAM126A^{A103R}). For all treatments, BRET values were normalized relative to an internal basal BRET control (PM-PI4KA^{BRET} biosensor expressed without the empty vector or EFR3B-P2A-TTC7B-T2A-FAM126A plasmid added) and are presented as the summary of triplicate wells measured for each treatment condition in three independent biological replicates (n = 3, with normalized signals from 9 total wells averaged). Normalized BRET signals were then expressed and graphed as fold-increases relative to the 100 ng/well pcDNA3.1 control.

1136 **C.** Representative confocal images of live HEK293A cells co-expressing a fixed amount (250 ng) of
1137 EGFP-PI4KA (greyscale) together with the indicated constructs (500 ng/each). The sequence and
1138 colour-coding of the experimental treatments are matched with the BRET measurements in (**B**).
1139
1140
1141
1142
1143
1144
1145
1146
1147
1148
1149
1150
1151
1152
1153
1154
1155
1156
1157
1158
1159
1160
1161
1162
1163
1164
1165
1166
1167
1168
1169
1170
1171
1172
1173
1174
1175
1176
1177
1178

Supplementary Figures and Tables

A

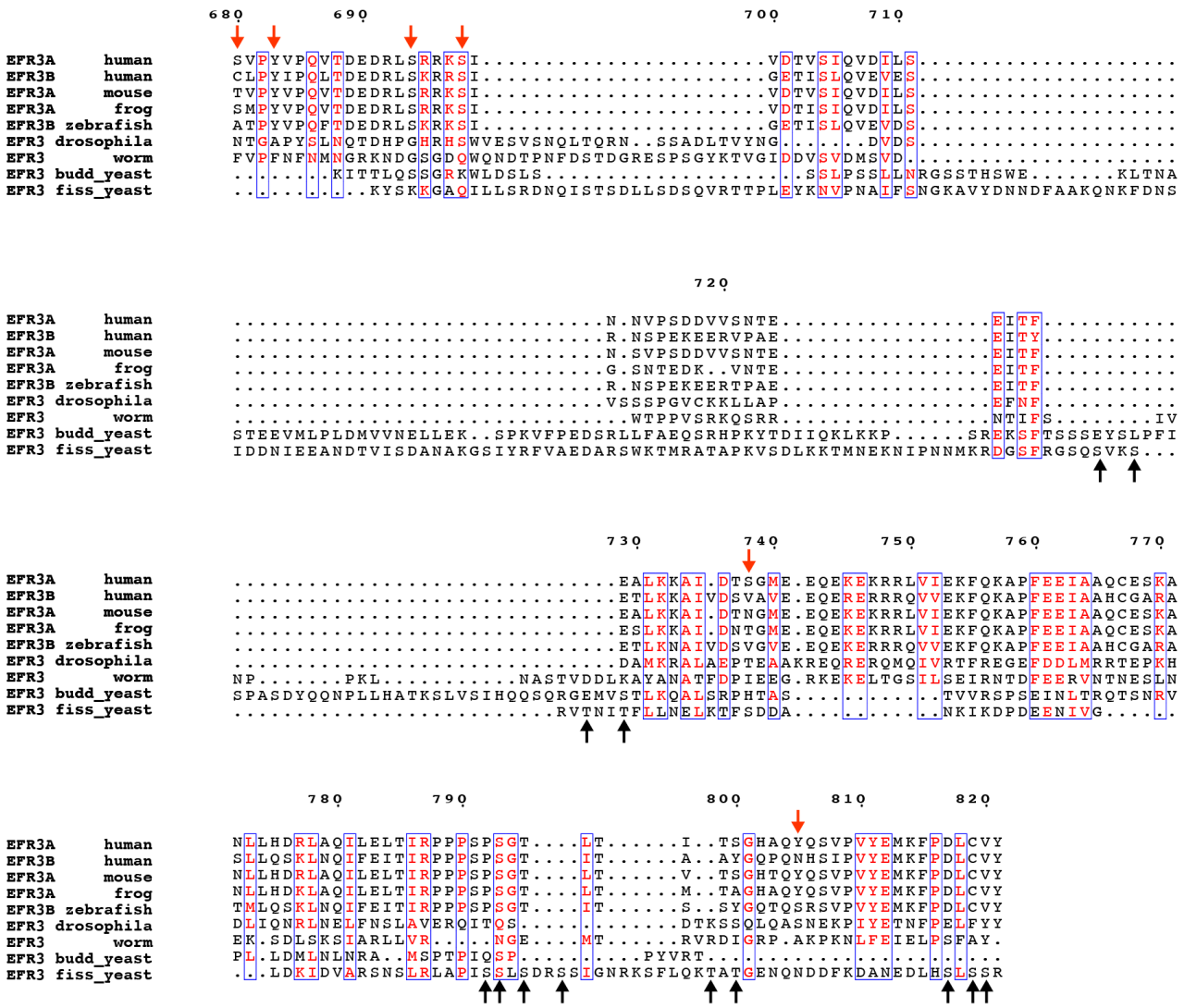

Supplemental Figure 1: EFR3 C-terminal tail sequence alignment

A. Multiple sequence alignment (generated with ESPript 3.0) of EFR3 from *Homo sapiens, Mus musculus, Xenopus laevis, Danio rerio, Drosophila melanogaster, Caenorhabditis elegans*, *Schizosaccharomyces pombe,* and *Saccharomyces cerevisiae.* Human EFR3A residues that are reported phosphorylation sites (Phosphosite) are annotated above in red. Yeast efr3 residues that are reported phosphorylation sites (PhosphoGRID) are annotated below in black.

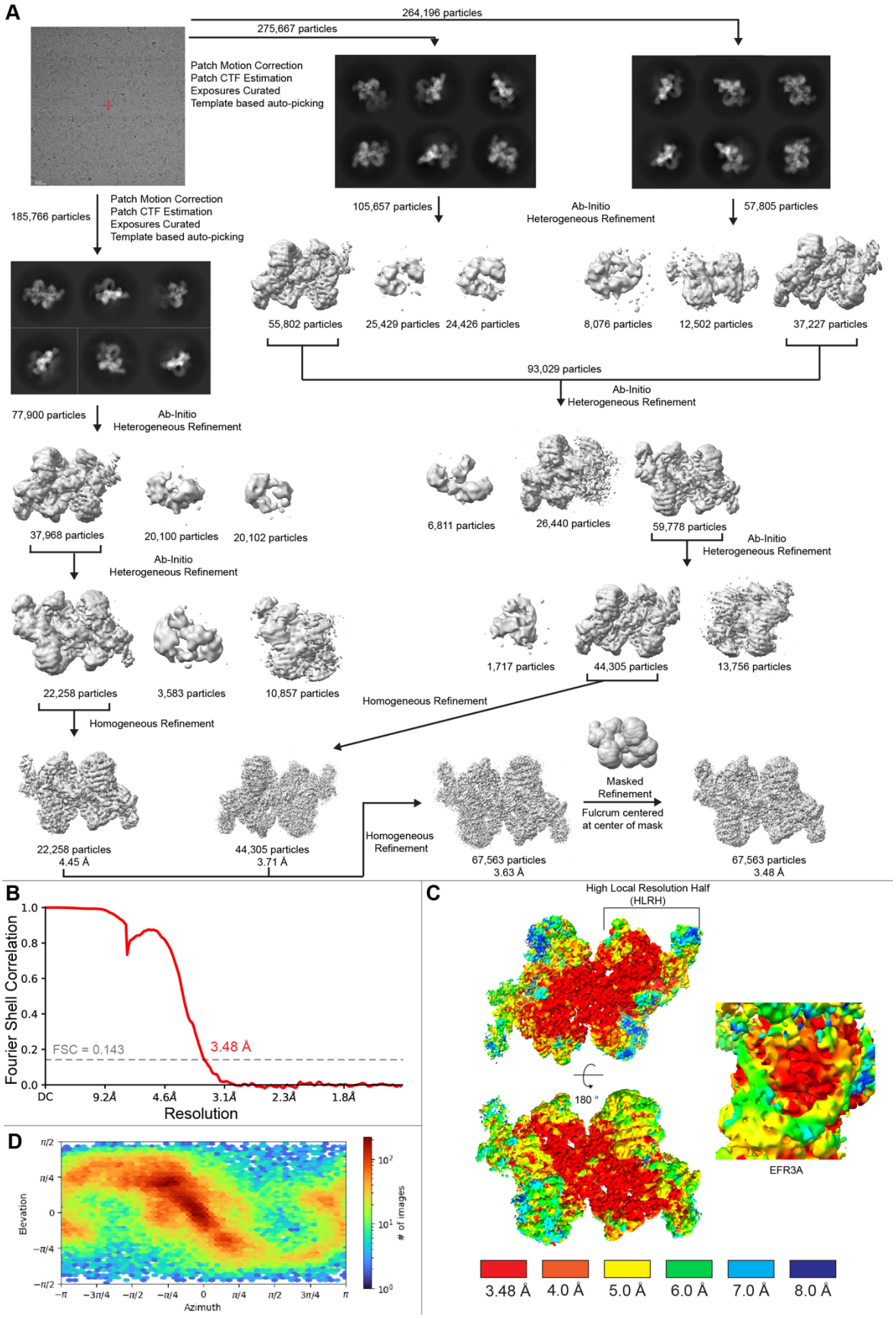
A
264,196 particles
275,667 particles
Patch Motion Correction
Patch CTF Estimation
Exposures Curated
Template based auto-picking
185,766 particles
Patch Motion Correction
Patch CTF Estimation
Exposures Curated
Template based auto-picking
105,657 particles
Ab-Initio
Heterogeneous Refinement
57,805 particles
55,802 particles
25,429 particles
24,426 particles
8,076 particles
12,502 particles
37,227 particles
93,029 particles
Ab-Initio
Heterogeneous Refinement
77,900 particles
Ab-Initio
Heterogeneous Refinement
37,968 particles
20,100 particles
20,102 particles
6,811 particles
26,440 particles
59,778 particles
Ab-Initio
Heterogeneous Refinement
Ab-Initio
Heterogeneous Refinement
22,258 particles
3,583 particles
10,857 particles
1,717 particles
44,305 particles
13,756 particles
Homogeneous Refinement
Homogeneous Refinement
22,258 particles
4.45 Å
44,305 particles
3.71 Å
Homogeneous
Refinement
67,563 particles
3.63 Å
Masked
Refinement
Fulcrum centered
at center of mask
67,563 particles
3.48 Å
B
Fourier Shell Correlation
FSC = 0.143
3.48 Å
DC
9.2Å
4.6Å
3.1Å
2.3Å
1.8Å
Resolution
C
High Local Resolution Half
(HLRH)
180 °
EFR3A
3.48 Å
4.0 Å
5.0 Å
6.0 Å
7.0 Å
8.0 Å
D
Elevation
Azimuth
# of images

1187

Supplemental Figure 2 (related to Fig.1): Cryo-EM data processing

A. Cryo-EM data processing workflow showing a representative micrograph from screening on the 200 kV Glacios, representative 2D class averages, and the image processing strategy used to generate a 3D reconstruction of the PI4KA/TTC7B/FAM126A/EFR3A complex.

B. Gold standard Fourier shell correlation coefficient (FSC) curve after auto tightening by cryoSPARC for the final map.

C. Final map coloured according to local resolution estimated using cryoSPARC v4.2.1, with a zoom-in of the EFR3A density.

D. Viewing direction distribution plot of particles in the final cryo-EM reconstruction output by cryoSPARC v4.2.1.

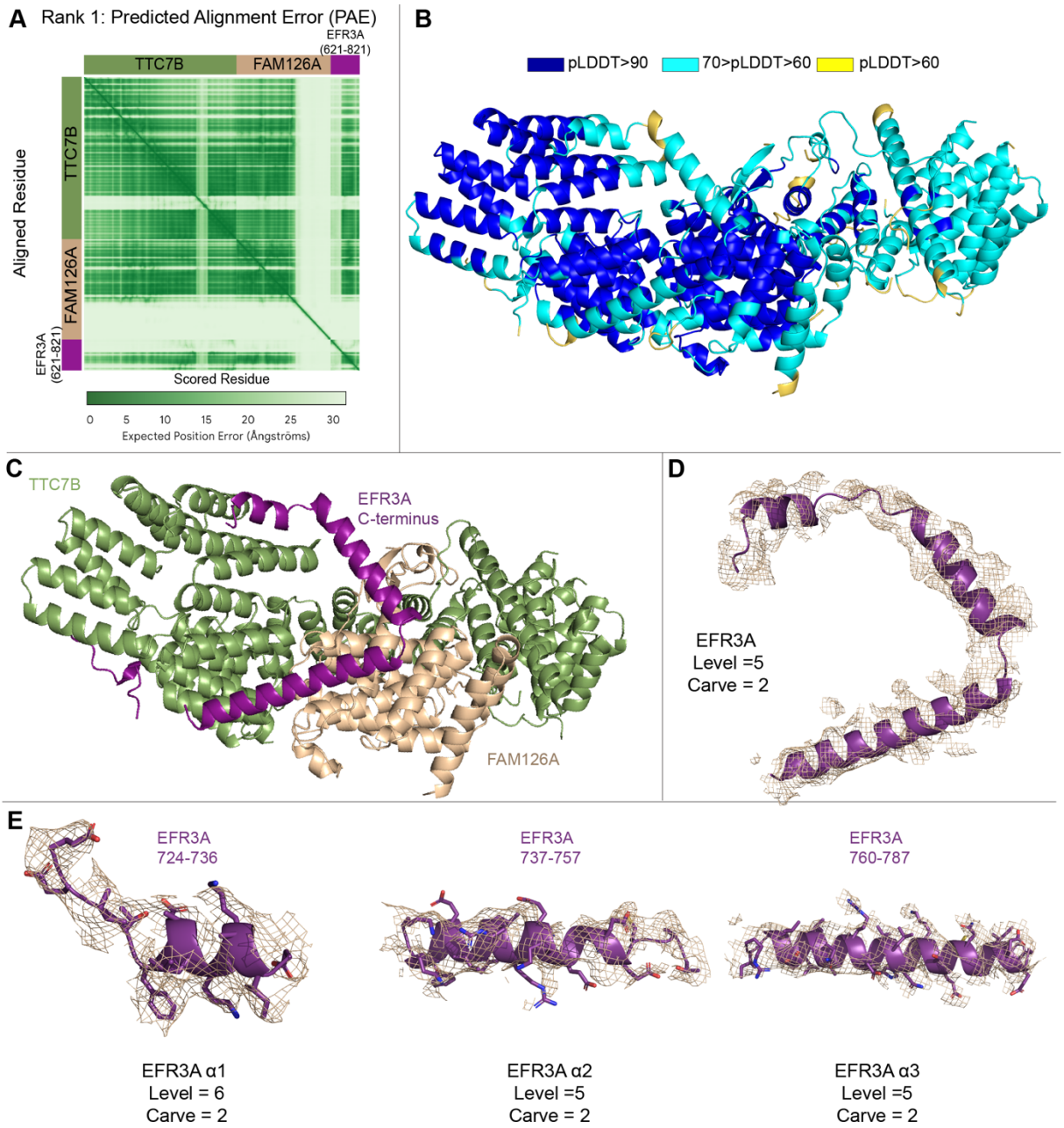

Supplemental Figure 3: Model building with AlphaFold Multimer and map to model density fit
A. Predicted aligned error (PAE) of the AlphaFold3 prediction of the TTC7B-FAM126A and EFR3A C-terminus.
B. AlphaFold3 model of TTC7B-FAM126A in complex with the EFR3A C-terminus with the per-residue confidence metric predicted local-distance difference test (pLDDT) <60 removed, coloured according to pLDDT score.
D. AlphaFold3 model of the TTC7B-FAM126A in complex with EFR3A C-terminal with the per-residue confidence metric predicted local-distance difference test (pLDDT) <60 removed.
E. Electron density of EFR3A C-terminus.
F. Electron density of selected regions. (L) EFR3A α1 with density for EFR3A (724-736) shown on top, and (M) EFR3A α2 with density for EFR3A (737-759), and (R) EFR3A α3 with density for EFR3A (760-787) shown.

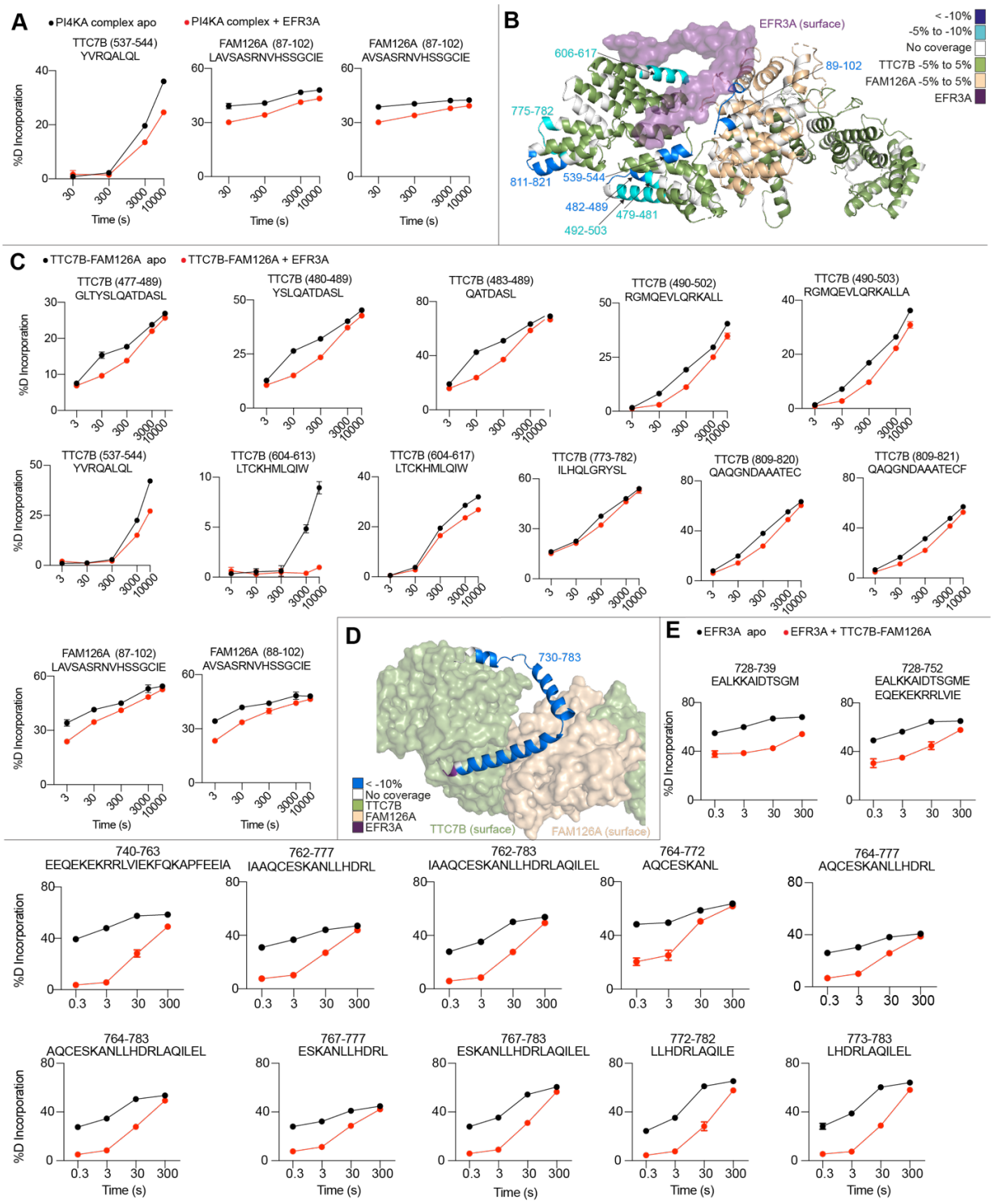

Supplemental Figure 4: Raw HDX-MS deuterium incorporation curves

A. Relative deuterium incorporation traces for peptides showing significant differences in deuterium exchange (defined as >5% >0.45 Da, and p<0.01 in an unpaired two-tailed t-test at any time point) upon PI4KA complex binding to EFR3A.

B. Significant differences in deuterium exchange (defined as >5% >0.45 Da, and p<0.01 in an unpaired two-tailed t-test at any time point) upon TTC7B-FAM126A dimer binding to EFR3A mapped on the high resolution half of our structural model with all regions annotated.

1224 **C.** Relative deuterium incorporation traces for peptides showing significant differences in deuterium
1225 exchange (defined as >5% >0.45 Da, and p<0.01 in an unpaired two-tailed t-test at any time point) upon
1226 TTC7B-FAM126A dimer binding to EFR3A.
1227 **D.** Significant differences in deuterium exchange (defined as >5% >0.45 Da, and p<0.01 in an unpaired
1228 two-tailed t-test at any time point) upon MBP-EFR3A binding to the TTC7B-FAM126A dimer mapped on
1229 the high resolution half of our structural model with all regions annotated.
1230 **E.** Relative deuterium incorporation traces for peptides showing significant differences in deuterium
1231 exchange (defined as >5% >0.45 Da, and p<0.01 in an unpaired two-tailed t-test at any time point) upon
1232 MBP-EFR3A binding to the TTC7B-FAM126A dimer.
1233
1234
1235
1236
1237
1238
1239
1240
1241
1242
1243

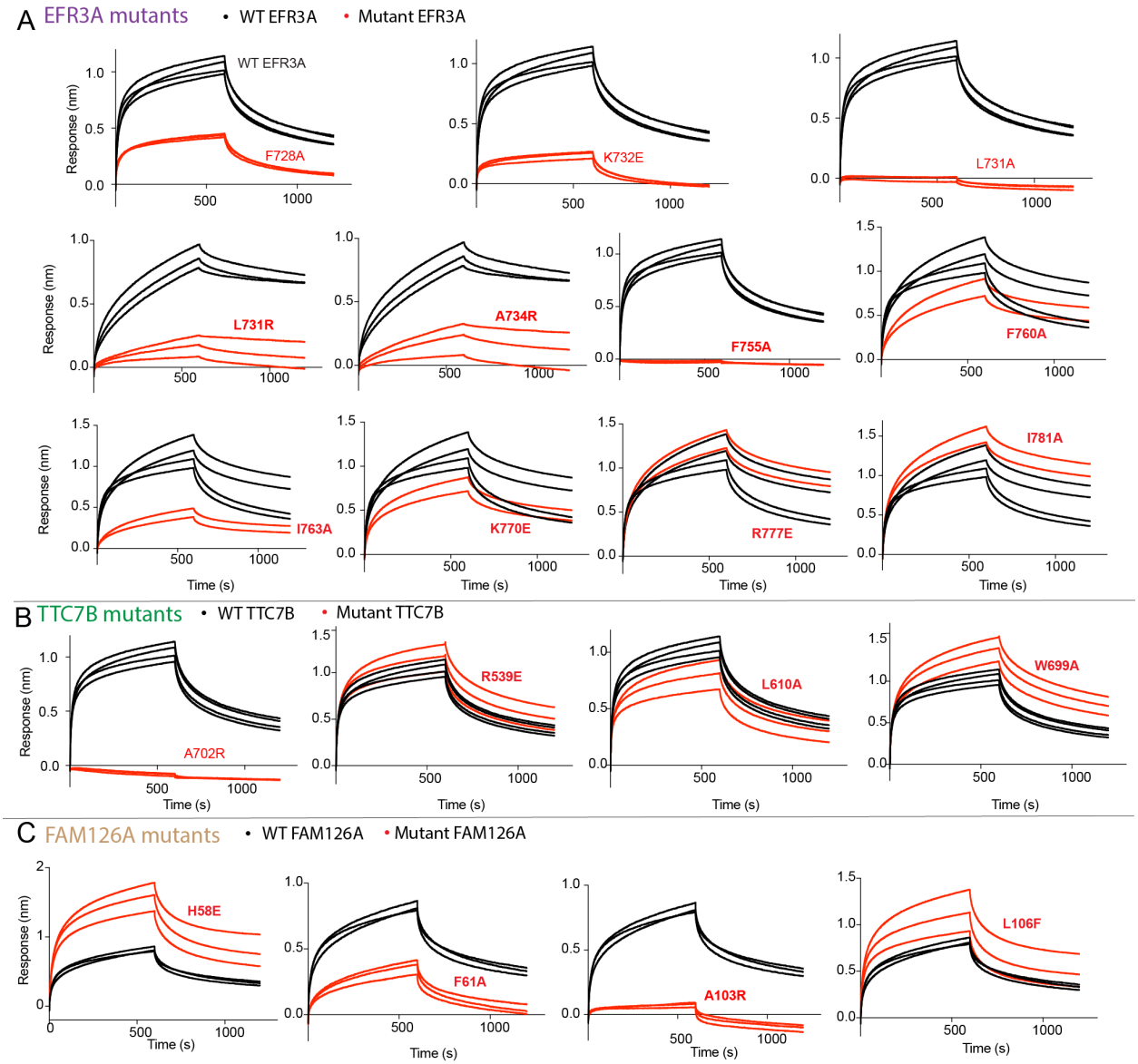

Supplemental Figure 5: BLI raw data

A. Raw BLI association and dissociation curves of all EFR3A mutants (shown in table S2) compared to WT. His-EFR3A was loaded on the anti-penta-His tip at 200 nM and dipped in TTC7B-FAM126A at 500 nM.
B. Raw BLI association and dissociation curves of all TTC7B mutants (shown in table S2) compared to WT. His-EFR3A was loaded on the anti-penta-His tip at 200 nM and dipped in TTC7B-FAM126A at 500 nM.
C. Raw BLI association and dissociation curves of all TTC7B mutants (shown in table S2) compared to WT. His-EFR3A was loaded on the anti-penta-His tip at 200 nM and dipped in TTC7B-FAM126A at 500 nM.

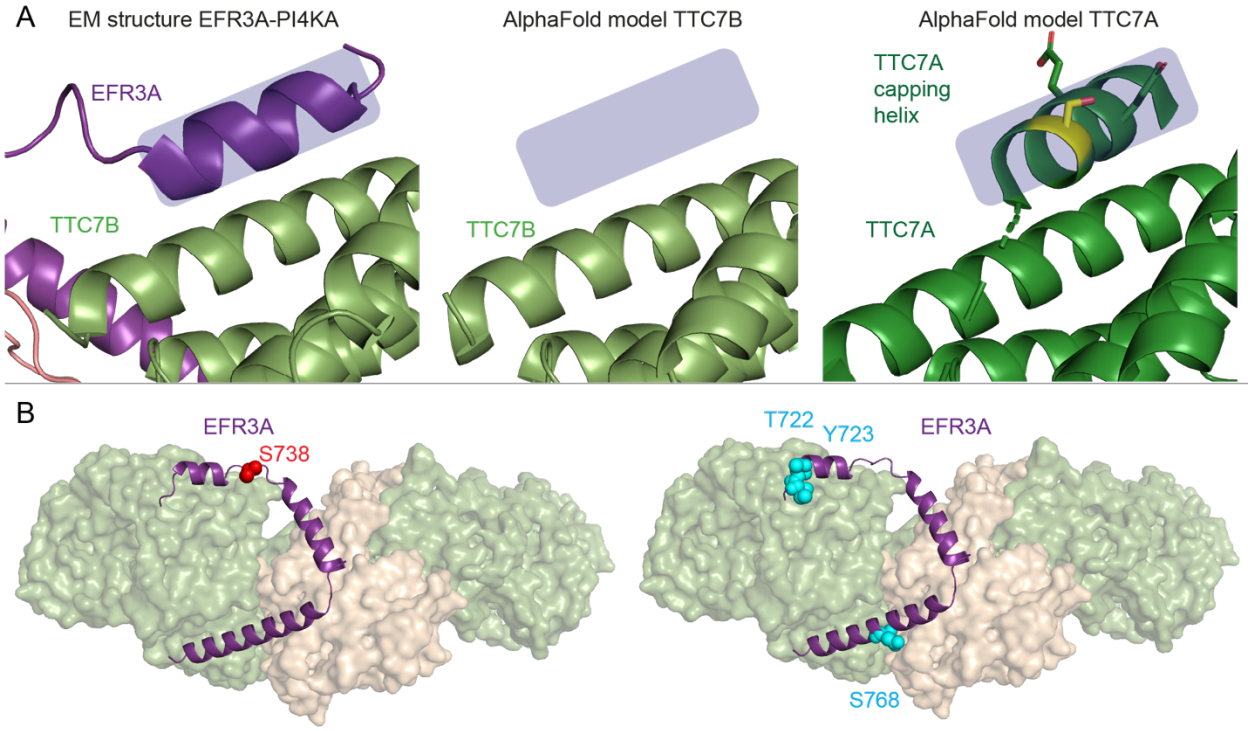

Supplemental Figure 6: Differences between TTC7A/TTC7B and post-translational modification sites present at the EFR3-TTC7-FAM126 interface

A. The structure of the α1 helix of EFR3A bound to TTC7B is shown on the top left. The AlphaFold models of TTC7B (middle) and TTC7A (right) are shown with all very low confidence regions (pLDDT values less than 50 being removed). AlphaFold predicts a capping helix in TTC7A at this binding interface, which has a reported phosphorylation site (Phosphosite) at S690 (colored yellow in the right panel). Additional reported TTC7A phosphorylation sites (Phosphosite) near this site are in predicted unstructured regions including S647, S678, S679, and T693.

B. (L) EFR3A and (R) EFR3B phosphorylation sites (Phosphosite) mapped on the cryo-EM model of PI4KA complex-EFR3A C-terminus.

1285 **Table S1 Cryo-EM data collection, refinement, and validation statistics**

	PI4KA/TTC7B/FAM126A (1-308)-EFR3A C-terminus EMD- 44413 PDB:9BAX
Data collection and processing	
Magnification	165,000
Voltage (kV)	300
Electron exposure (e/ Å^2)	50
Defocus range (μM)	0.5-2.0
Pixel size (Å)	0.77
Symmetry imposed	C1
Initial particle images (no.)	725,629
Final particle images (no.)	67,563
Map resolution (Å)	3.63
FSC threshold	0.143
Map resolution range (Å)	3.3-10
Refinement	
Initial model used (PDB)	6BQ1/AlphaFold3
Model Resolution (Å)	3.48
FSC threshold	0.143
Map sharpening B factor	
Model composition	
Non-hydrogen atoms	40637
Protein residues	5082
Ligands	0
B-factors	
Protein	242
Validation	
Mol probability score	1.97
Clashscore	8.65
Poor rotamers (%)	1.48
Ramachandran	
Favoured	94.50
Allowed	5.48
Outliers	0.02
R.M.S. deviations	
Bond lengths (Å)	0.004
Bond angles (°)	0.565

1286
1287
1288
1289

1290 **Table S2 Key Reagent/Resources**

REAGENT or RESOURCE	SOURCE	IDENTIFIER
Bacterial and virus strains		
E.coli XL10-GOLD KanR Ultracompetent Cells	Agilent	200317
E.coli DH10EMBacY Competent Cells	Geneva Biotech	DH10EMBacY
C41(DE3) chemically competent cells	Lab stock	
Chemicals, peptides, and recombinant proteins		
Deuterium Oxide 99.9%	Sigma Aldrich	151882-10X1ML
BS^3	Thermo Fischer Scientific	21580
ATP	Sigma	A7699-1g
$MgCl_2$	Caledon Laboratory Chemicals	4720-1
Deposited Data		
Mass spectrometry proteomics data	https://www.ebi.ac.uk/pride/	PXD043442
PDB	https://www.rcsb.org/	9BAX
EMDB	https://www.emdataresource.org/	44413
Recombinant DNA		
PI4KA Complex	Dornan et al., 2018	GD177
EFR3A (721-791)	This paper	SS77
MBP-EFR3A (721-791)	This paper	MJ319
EFR3A (F728A)	This paper	SS88
EFR3A (L731A)	This paper	SS99
EFR3A (L731R)	This paper	SS140
EFR3A (L734R)	This paper	SS141
EFR3A (K732E)	This paper	SS89
EFR3A (F755A)	This paper	SS90
EFR3A (F760A)	This paper	SS91
EFR3A (I763A)	This paper	SS102
EFR3A (K770E)	This paper	SS92
EFR3A (R777E)	This paper	SS93
EFR3A (I781A)	This paper	SS94
TTC7B-FAM126A (1-308) WT	Dornan et al., 2018	GD176
TTC7B-FAM126A (1-308) WT – *E.coli*	This paper	AS29
TTC7B (A702R)-FAM126A (1-308)	This paper	MS8
TTC7B (R539E)-FAM126A (1-308)	This paper	SS115
TTC7B (L610A)-FAM126A (1-308)	This paper	SS113
TTC7B (W699A)-FAM126A (1-308)	This paper	SS116
TTC7B-FAM126A (H58E) (2-308)	This paper	SS104
TTC7B-FAM126A (F61A) (1-308)	This paper	SS103
TTC7B-FAM126A (A103R) (1-308)	This paper	MS4
TTC7B-FAM126A (L106F) (1-308)	This paper	SS105
EFR3Bha_gsgT2A_TTC7Bmyc_FlagFam126A	This paper	C3
EFR3Bha_t2a_TTC7B myc_p2a_Flag FAM126A (A103R)	This paper	NH74
EFR3Bha_t2a_TTC7B (A702R) myc_p2a_Flag FAM126A	This paper	NH75

EFR3Bha ∆c-term (1-715)_gsgT2A_TTC7Bmyc_FlagFam126A	This paper	NH93
EFR3Bha(L726A, F751A)_gsgT2A_TTC7Bmyc_FlagFam126A	This paper	NH94
EGFP-PI4KA	Hammond et al., 2014	
L10-mVenus-tPT2A-nLuc-PI4KA	This paper	PM-PI4KA^{BRET}
Software and algorithms		
cryoSPARC v4.2.1	Structura Bio	https://cryosparc.com
Phenix-1.19.1	Open source	https://phenix-online.org/
COOT-0.9.4.1	CCP4	https://www2.mrc-lmb.ca
HDExaminer	Sierra Analytics	http://massspec.com/hdexaminer
Bruker Compass DataAnalysis 4.2	Bruker	http://www.bruker.com
GraphPad Prism 7.0	GraphPad	https://www.graphpad.com
PEAKS 7	Bioinformatics Solutions Inc.	https://www.bioinfor.com/versions/
FragPipe (v19.1)	Nesvizhskii Lab – University of Michigan	fragpipe.nesvilab.org
Adobe Illustrator 2021	Adobe	https://www.adobe.com/products/illustrator.html
ESPript 3.0	SBGrid consortium	https:espript.ibcp.fr
PyMOL	Schroedinger	http://pymol.org
ChimeraX	UCSF	https://www.cgl.ucsf.edu/chimerax/
Other		
C-flat Holey Thick Carbon Grid 2.0 μm hole 1.0 μm space 300 mesh	Electron Microscopy Studies	CFT312-100
SF9 insect cells for expression	Expression Systems	94-001S
Octet HIS1K Biosensors	Sartorius	18-5120
Enzymate Protein Pepsin Column, 300Å, 5μm, 2.1 mm X 30 mm	Waters	186007233
ProDx Pepsin Column F 10-32	Trajan Scientific Americas	359997870
ACQUITY UPLC BEH C18 1.7 μm, 2.1 mm x 5 mm	Waters	186004629
ACQUITY UPLC Peptide BEH C18 Column, 300Å, 1.7 μm, 100 mm X 2.1 mm	Waters	186003686

1291